Aging affects reprogramming of murine pulmonary capillary endothelial cells after lung injury

Marin Truchi[1#], Marine Gautier-Isola[1#], Grégoire Savary[2#], Hugo Cadis[1], Célia Scribe[1], Alberto Baeri[1], Arun Lingampally[3], Virginie Magnone[1], Cédric Girard-Riboulleau[1], Marie-Jeanne Arguel[1], Clémentine de Schutter[2], Julien Fassy[1], Nihad Boukrout[2], Romain Larrue[2], Nathalie Martin[2], Roger Rezzonico[1], Olivier Pluquet[2], Michael Perrais[2], Véronique Hofman[4], Charles-Hugo Marquette[5], Paul Hofman[4], Andreas Günther[6,7], Nicolas Ricard[8], Pascal Barbry[1], Sylvie Leroy[1,5], Kevin Lebrigand[1], Saverio Bellusci[3], Christelle Cauffiez[2], Georges Vassaux[1], Nicolas Pottier[2#] and Bernard Mari[1*#]

[1]*Université Côte d'Azur, UMR CNRS 7275 Inserm 1323, IPMC, FHU-OncoAge, IHU RespiERA, Valbonne, France*

[2]*Univ. Lille, CNRS, Inserm, CHU Lille, Institut Pasteur de Lille, UMR9020 CNRS - U1277 Inserm - CANTHER, Lille, France.*

[3]*Excellence Cluster Cardio-Pulmonary System, German Center for Lung Research, Justus-Liebig-University Giessen, Giessen, Germany*

[4]*Université Côte d'Azur, Laboratory of Clinical and Experimental Pathology and Hospital-Integrated Biobank (BB-0033-00025), CHU Nice, FHU OncoAge, IHU RespiERA, Nice, France*

[5]*Département de Pneumologie, FHU-OncoAge, IHU RespiERA, CHU-Nice, France*

[6]*Center for Interstitial and Rare Diseases and Cardiopulmonary Institute, Justus-Liebig-University Gießen, Giessen, Germany*

[7]*European IPF Registry and Biobank*

[8]*Laboratory BioSanté U1292, Univ. Grenoble Alpes, INSERM, CEA, 38000, Grenoble, France*

[#]Contributed equally

[*]Correspondence to Bernard Mari, Institut de Pharmacologie Moléculaire et Cellulaire, CNRS-UMR-7275, Université Côte d'Azur, 660 route des Lucioles, F-06560. Email: mari@unice.fr

ABSTRACT

Aging increases the risk of developing fibrotic diseases by hampering tissue regeneration after injury. Using longitudinal single-cell RNA-seq and spatial transcriptomics, here we compare the transcriptome of bleomycin-induced fibrotic lungs of young and aged mice, at 3 time points corresponding to the peak of fibrosis, regeneration and resolution. We find that lung injury shifts the transcriptomic profiles of three pulmonary capillary endothelial cells (PCEC) subpopulations. The associated signatures are linked to pro-angiogenic signaling with strong *Lrg1* expression and do not progress similarly throughout the resolution process between young and old animals. Moreover, part of this set of resolution-associated markers is also detected in PCEC from samples of patients with idiopathic pulmonary fibrosis. Finally, we find that aging also alters the transcriptome of PCEC which display typical pro-fibrotic and pro-inflammatory features. We propose that age-associated alterations in specific PCEC subpopulations may interfere with the process of lung progenitor differentiation, thus contributing to the persistent fibrotic process typical of human pathology.

INTRODUCTION

Gas exchanges between the external environment and the cardiovascular system take place in the lung alveoli through the thin membrane separating alveolar epithelial cells (AEC) and the capillary plexus formed by pulmonary capillary endothelial cells (PCEC), supported by mesenchymal cells. This alveolar niche, whose homeostasis is constantly threatened by external aggressions, deploys high regeneration abilities through various mechanisms[1]. Inadequate responses can lead to the development of chronic diseases such as idiopathic pulmonary fibrosis (IPF), an age-related pathology characterized by the accumulation of collagen-producing mesenchymal cells (myofibroblasts) resulting in the remodeling of the alveolar environment and accumulation of extracellular matrix (ECM), leading to progressive destruction of the parenchyma[2]. IPF is the prototypical progressive interstitial lung disease (ILD) associated with progressive decline in lung function and a median survival time of less than five years after diagnosis. Although two treatments are available to manage the disease (ie: nintedanib and perfenidone) and several new therapeutic options are under investigation, there is no curative treatment for IPF to date[3]. The pathogenesis of IPF is complex and largely unknown. Current hypotheses suggest that repetitive microinjuries of unknown origin to AEC in the aging lung results in ineffective repair with excessive wound healing, chronic inflammation, apoptosis of AEC and endothelial cells (EC), activation of fibrogenic effector cells, formation of myofibroblasts foci, and finally excessive deposition of ECM resulting in the destruction of the lung architecture and the loss of lung functions[4]. Mechanisms linking aging to the development of pulmonary fibrosis are not fully understood and involve numerous cell-intrinsic and cell-extrinsic alterations. Among them, it has been proposed that genetic and epigenetic changes, loss of proteostasis, cellular senescence, metabolic dysfunction as well as stem cell exhaustion may contribute to the initiation and progression of fibrosis[5-7].

Following lung injury, the restoration of parenchymal tissue integrity depends in particular on the proliferative capacities of PCEC[8]. Recent studies showed that, in physiological conditions, PCEC are functionally heterogeneous, with two distinct cell types conserved in multiple mammal species[9]. Aerocytes (aCap), are specialized in gas exchanges with type 1 AEC (AEC1), whereas general capillaries (gCap) act as progenitor-like cells able to self-renew and to differentiate into aCap to maintain the homeostasis of the microvascular endothelium. Multiple studies also report various EC subpopulations emerging after lung injury in mouse models[10-12] or in the context of IPF[13]. In particular, a population of peri-bronchial venous ECs expressing COL15A1, and referred as “systemic venous” (SV EC), have been shown to expand in areas of bronchiolization and fibrosis in IPF patient while this EC subtype was restricted to the bronchial vasculature in healthy lungs[13, 14]. A recent study[15] further characterized these COL15A1^{pos} systemic ECs in lungs from lethal COVID-19 and IPF patients and identified a second subpopulation lacking expression of venous marker genes while

85 expressing markers commonly detected in gCap, referred as systemic capillary ECs (sCap).
86 Nevertheless, the precise contribution of the physiological state-associated cell types in the
87 formation of these pathological subpopulations is not fully known. Moreover, as the
88 regenerative functions of EC decline with aging[16, 17], the impact of aging on the dynamic of EC
89 subpopulations associated with alveolar niche regeneration after injury-induced fibrosis
90 remains largely unaddressed[18].
91 The murine single intratracheal bleomycin instillation model is considered as the best-
92 characterized animal model available for the preclinical assessment of potential therapies for
93 pulmonary fibrosis[19]. After the acute inflammatory phase has subsided, bleomycin-instilled
94 mice display AEC remodeling and fibrosis, but unlike patients with IPF, fibrosis progressively
95 resolves, allowing to study the cellular and molecular mechanisms associated with alveolar
96 repair and regeneration. Furthermore, studies assessing the response of older mice to
97 bleomycin have revealed a more pronounced fibrosis, with mechanisms more reminiscent of
98 IPF[20-22]. It has been notably suggested that fibrosis resolution or tissue regeneration is
99 impaired in aged mice[23-26] indicating that age-associated processes contribute to the persistent
100 fibrosis that is observed in IPF.
101 In this context, the aim of the present study was to compare the fate of different cell populations
102 present in the lungs after bleomycin-induced injury in young and aged animals, from the fibrotic
103 response peak (14 days) until partial (28 days) and complete (60 days) resolution.
104
105 **RESULTS**
106 **Aging is associated with a delay in the resolution of lung fibrosis**
107 Lungs of young (7 weeks) and old (18 months) mice were collected 14, 28 or 60 days after
108 bleomycin challenge (**Fig. 1A**). We noticed a shift of fibrosis resolution between young and
109 aged mice, as visualized by total hydroxyproline assay (**Fig. 1B**), histological analyses (**Fig.
110 1C**) and Sirius red assay (**Supplemental Fig. S1A**) with a peak of fibrosis at day 14 in young
111 mice followed by a progressive reduction of fibrosis at D28 while a strong fibrotic pattern was
112 still detected at D28 in old mice. In both young and old animals, fibrosis resolution was almost
113 complete at D60, with only a few limited fibrotic areas. We then performed a spatial
114 transcriptomics experiment with the 10x Genomics Visium platform on lung sections from
115 young or old mice taken 14 or 28 days after bleomycin instillation to compare the fibrotic and
116 resolution stages between the two age groups (**Fig. 1D**). After filtering the genes and the low-
117 quality spots, we processed the data, corresponding to a corpus of 2479 genes x 10813 spots
118 count matrix and the associated spatial coordinates, using a deconvolution tool leveraging only
119 on spatial gene expression profiles[27]. We identified 14 unique topics, *i.e.* modules of covarying
120 genes proportionally represented in each spot and annotated them according to their
121 differentially expressed genes (**Supplemental Fig. S1B-C and Supplementary table S1**).

122 Canonical pathway enrichment (**Fig. 1E)** and correlation analysis (**Supplemental Fig. S1D)**
123 revealed similarity between topics, with topics related to fibrotic tissue (topics 1, 13-14),
124 regenerative or normal alveoli (4-6) or immune cells extravasation, immunoglobin and antigen
125 presentation signaling (8 and 12). We then compared the average proportion of each topic in
126 all spots of each lung section, indicating at day 14 large areas of fibrosis, enriched in fibroblast
127 and macrophage markers (topics 1, 13-14) in lungs from both young and aged mice (**Fig. 1F**).
128 At D28, lungs from young mice and, to a lesser extent, from aged mice, showed a reduced
129 representation of topics related to fibrotic tissue compared to D14 while the areas
130 corresponding to regenerative or normal alveoli (4-6) showed an opposite trend. Lung sections
131 of old mice were also specifically enriched for the topic 8 (antigen presentation signaling),
132 suggesting that infiltration of immune cells such as plasma cells, known to form aggregates in
133 both IPF and the bleomycin model[28, 29], is exacerbated by aging during fibrosis resolution.
134 Overall, using various approaches, our data indicated that fibrosis resolution is delayed in lungs
135 from aged mice.
136
137 **Time-resolved scRNA-seq captures cellular heterogeneity of bleomycin-injured lungs**
138 **from young and aged mice.**
139 We reproduced the same experiment and performed scRNA-seq (10x Genomics Chromium
140 platform) on whole lungs of young (7 weeks) and aged (18 months) mice (n=3) collected 14,
141 28 or 60 days after bleomycin challenge or PBS (**Fig. 2A**). The samples of both conditions
142 from each time point were multiplexed using cell hashing[30] to mitigate batch effects. The count
143 matrices from the 36 sequenced samples were integrated to obtain a single dataset of 44,541
144 cells (**Supplemental Fig. S2A-B**). Based on their transcriptomic profile, cells were clustered
145 and manually annotated based on the expression of specific gene markers (**Fig. 2B,**
146 **Supplemental Fig. S2C and Supplementary table S2**). We identified 41 populations
147 recapitulating the cellular heterogeneity of the mouse lung, of which 29 were immune cells
148 from lymphoid or myeloid lineage, such as alveolar macrophages (AMs). We also detected
149 mesenchymal cells, including fibroblasts, pericytes, mesothelial cells as well as epithelial
150 populations such as AT1, AT2 and bronchial multiciliated cells. We finally identified 6 EC
151 populations: proliferating EC (Prolif. EC), gCap, aCap, pulmonary-venous EC (PV EC), arterial
152 EC and lymphatic EC. As expected, we observed a shift in several populations following
153 bleomycin injury (**Fig. 2C and Supplementary table S3**). This was particularly the case for
154 macrophages, as previously described [31-33], with a rapid influx of recruited monocyte-derived
155 macrophages (Mo-AMs) AM3 populations along with a drop of the tissue-resident (TR-AMs)
156 AM1 (**Supplemental Fig. S2D**). We evaluated the impact of age on the frequency of each AMs
157 subpopulation relatively to the total number of cells analyzed in each mouse treated with PBS
158 or BLM (**Supplemental Fig. S2E-F**). Overall, bleomycin treatment induced a very similar

159 dynamics of macrophage subsets in young and old animals from the peak of fibrosis to
160 complete resolution indicating that none of these specific subpopulations are associated with
161 the delayed resolution in aged animals. Remarkably, bleomycin injury also induced major
162 alterations in pulmonary EC types, especially gCap, PV EC and aCap (**Fig. 2C**), suggesting
163 underlying cellular heterogeneity in bleomycin-treated mice.
164
165 **Lung injury shifts PCEC towards Lrg1^{pos} subpopulations**
166 The subclustering of PCEC and macrovascular subsets revealed the emergence of four new
167 subpopulations in bleomycin-injured lungs from both young and aged mice (**Fig. 2D**). Among
168 these subclusters, two new subpopulations of gCap and aCap cells emerged in fibrotic lungs
169 with recognizable signatures particularly characterized by the overexpression of Leucine-rich
170 α-2 glycoprotein 1 (*Lrg1*) and mostly found at day 14 and day 28 following bleomycin treatment
171 (**Fig. 2E-F, Supplemental Fig. S3A and Table 1**). The third population matched a cluster of
172 proliferating PCEC (Prolif. EC), which was only found at day 14 and to a lesser extent at day
173 28 following bleomycin treatment (**Fig. 2E** and **Supplementary table S2**). A fourth population
174 expressed the "SV EC" marker Col15a1, an ectopic population, recently found widespread in
175 fibrotic areas of IPF patients[13]. In order to establish a link between the endothelial remodeling
176 induced after lung injury in the mouse model and human IPF, we re-analyzed the pulmonary
177 endothelial subset from the Habermann dataset [34] (IPF Cell atlas), confirming the increase of
178 the *COL15A1*-positive systemic EC (previously annotated as "SV EC") proportion at the
179 expense of others cell types in lungs from transplanted patients with IPF compared to healthy
180 donors (**Fig. 2G-I).** The *Col15a1*^{pos} murine population shared, to some extent, the expression
181 of others markers found in human systemic EC, such as *Hspg2, Nrp2, Gja1, Vwa1, Lamb1,*
182 *Spry1, Filip1, Ndrg1, Nr5a2, Galnt15* and *Meox1* (**Fig. 2J-K and Supplementary table S4**).
183 However, this population, described as being of macrovascular origin, doesn't express
184 macrovascular markers such as *Vwf* or *Vcam1* and also lacks expression of venous markers
185 (Ackr1). Instead, the Col15a1^{pos} murine population shares several gCap markers such as *Aplnr*
186 or *Sox11* (**Fig. 2F** and **Table 1**), confirming in mouse the identification of a systemic capillary
187 ECs (sCap) recently characterized in lungs from lethal COVID-19 and IPF patients[15]. *In situ*
188 hybridization confirmed the induction of *Col15a1* in BLM-treated mice (**Fig. 2L**), with a pattern
189 similar as that observed in fibrotic areas of lung IPF sections (**Fig. 2M**). We hence considered
190 these *Col15a1*^{pos} sCap as a distinct PCEC subpopulation for the rest of the study. On the other
191 hand, we observed a low expression of *LRG1* in systemic EC from IPF samples (Habermann
192 dataset[34]). We did not detect *LRG1* either in gCap or aCap from IPF samples, but decreased
193 *EDNRB* was observed in aCap, as in aCap from bleomycin-treated mice **(Fig. 2F-I)**.
194 We then analyzed the profile of *Lrg1* expression in lung cell types in both basal condition or
195 after BLM treatment in young and aged mice. In physiological condition, *Lrg1* expression is

196 restricted to the macrovascular *Col15a1*-negative pulmonary-venous (PV EC), neutrophils,
197 LCM, and to a lesser extent to AT2, gCap and Lymphatic EC **(Supplementary table S2** and
198 **supplemental Fig. S3B).** At the peak of fibrosis, *Lrg1* expression was dramatically increased
199 in all EC subpopulations as well as in alveolar macrophages subsets **(Supplemental Fig.**
200 **S3B)**. We confirmed this increase of *Lrg1* in bleomycin-treated lungs by *in situ* hybridization
201 **(Supplemental Fig. S3C)**. The kinetics of *Lrg1* expression in old versus young mice treated
202 with BLM was similar in most subpopulations, apart for gCap, aCap and Arterial EC, for which
203 *Lrg1* expression was time-shifted at day 28 **(Supplemental Fig. S3D).** Finally, overexpression
204 of *Lrg1* in gCap and aCap was validated on an independent scRNA-seq dataset[35] in which
205 lungs of adult mice treated with bleomycin were collected at a shorter time interval
206 **(Supplemental Fig. S3E).**
207
208 **Lrg1^{pos} PCEC signaling is associated with vascular remodeling and alveolar**
209 **regeneration.**
210 *LRG1* is a gene coding for a pro-inflammatory glycoprotein, which can notably promote
211 angiogenesis by switching TGF-β signaling from SMAD2/3 angiostatic signaling to SMAD1/5
212 angiogenic signaling[36]. To confirm this hypothesis, we generated a HMEC1 human endothelial
213 cell line constitutively overexpressing LRG1. Control and LRG1 vector transduced cells were
214 stimulated or not with TGF-β1 at 2 different concentrations (3 or 10 ng/ml). While in control
215 cells, TGF-β1 mostly induced phosphorylation of SMAD2/3, LRG1 expression preferentially
216 promoted SMAD1/5 phosphorylation at both low and high TGF-β1 concentrations
217 (**Supplemental Fig. S4A-D**). This switch was also accompanied with a significant increase of
218 *VEGF* transcript (**Supplemental Fig. S4E**), indicating that Lrg1^{pos}PCEC signaling may
219 participate in alveolar regeneration through induction of angiogenesis.
220 Ingenuity Pathway Analysis™ performed on *Lrg1*^{pos} PCEC markers indicated an activation of
221 mTOR, TGF-β, integrin-linked kinase and wound healing pathways in all 3 PCEC
222 subpopulations (**Fig. 3A)**. Enriched functions pointed to activation of angiogenesis or
223 vasculogenesis, EC migration and proliferation in all 3 PCEC subpopulations, which is lacking
224 or to a lesser extent in PV EC (**Fig. 3B)**. We also noted elevated expression of hypoxia-
225 regulated genes with *Lrg1*^{pos} aCap showing the strongest signature (**Fig. 3C)**. Expression of
226 markers associated with angiogenesis was shared by all three *Lrg1*^{pos} PCEC subpopulations,
227 in particular genes coding for ECM-associated proteins, transcription factors/regulators,
228 cytokines/growth factors and receptors. RNAscope™ FISH confirmed the expression of HIF1α
229 mRNA in *Lrg1*^{pos} cells in fibrotic areas, as well as increased expression of *Vegfa* and *Sox17* in
230 gCaps at the peak of fibrosis (**Fig. 3E**). suggesting a central role for *Lrg1*^{pos} PCEC in endothelial
231 regeneration processes via intense signaling within the alveolar niche (**Fig. 3D)**.

232 To follow up this hypothesis, we used NicheNet[37] to infer ligand-receptor interactions
233 potentially associated with the expression of genes related to the pro-angiogenic signature of
234 Lrg1^{pos} PCEC. We selected the top ligands with the highest probability to induce these pro-
235 angiogenic signatures in each Lrg1^{pos} PCEC subpopulation. Most of the selected ligands were
236 commonly prioritized in the 3 subpopulations and were known pro-angiogenic factors, such as
237 *Fgf2*, *Vegfa*, *Il1b*, *Tgfb1*, *Apoe*, *Bmp4*, *Adam17* or *Cxcl12* **(Supplemental Fig. S5A).** We next
238 looked at the expression of the selected ligands as well as the downstream genes most likely
239 to be regulated by these ligands in the different lung cell populations. Notably, *Vegfa* and
240 *Cxcl12* ligands were among the top predicted ligands as well as the top predicted downstream-
241 regulated genes, suggesting autocrine signaling within *Lrg1*^{pos} PCEC **(Supplemental Fig.**
242 **S5A)**. We finally checked the expression of genes encoding *bona fide* receptors of the selected
243 ligands in the 3 *Lrg1*^{pos} PCEC subpopulations (**Fig. 3F)**. Overall, their transcripts were
244 equivalently detected in the 3 *Lrg1*^{pos} EC subpopulations, with the exception of Fgf2 receptors
245 Fgfr1 and Fgfr3 which are more specific to the *Lrg1*^{pos} aCap. We have summarized these
246 interactions inferences in a circos plot, linking the selected ligands grouped by expression in
247 specific cell populations to their top receptors expressed in *Lrg1*^{pos} PCEC subpopulations (**Fig.**
248 **3G)**. We represented potential paracrine and autocrine signaling involving ligands expressed
249 by mast cells (*Hgf*), neutrophils (*Il1b*), macrophages (*Il1a*, *Adam17*, *Tnf* and *Apoe*) as well as
250 ligands expressed in multiple cell types such as *Tgfb1* and *Gpl1*. We also found potential
251 interactions between ligands of neighboring cell types within the alveolar niche and *Lrg1*^{pos}
252 PCEC receptors, such as the *Bmp4* / *Bmpr2* pair involving alveolar epithelial cells and the
253 *Tgfb3* / *Tgfbr2* pair with mesenchymal cells. Based on the hypothesis that a receptor
254 differentially expressed between physiological and fibrotic conditions likely indicates a
255 modulation of the associated signaling pathway, we then compared receptor expression levels
256 between gCap from bleomycin- versus PBS-treated mice. We observed that *Ackr3*, *Il1r1*, *Itgb1*,
257 *Nrp2*, *Scarb1*, *Sdc4* and *Tgfbr2* were all upregulated while *Bmpr2* and *Tgfbr3* were
258 downregulated in bleomycin-treated compared to control gCap **(Supplemental Fig. S5B)**.
259 These observations appear consistent in the context of capillary endothelial remodeling. For
260 example, the autocrine signaling pathway involving *Cxcl12* and *Ackr3* in PCEC has been
261 shown to drive AEC expansion and neo-alveolarization by releasing Mmp14 following lung
262 injury[38]. Our analysis indeed validated the upregulation of *Mmp14* in bleomycin-treated gCap
263 at the single cell transcriptomic level **(Supplemental Fig. S5C)**. Finally, other genes driving
264 key signal transduction proteins in EC, such as Eng, Id1 and several Smad family members,
265 were also differentially expressed between both conditions in gCap **(Supplemental Fig. S5C)**.
266 In particular, we found that *Smad6* was significantly downregulated in bleomycin-treated gCap.
267 Coupled with the repression of *Bmpr2* and a similar trend for other BMP9 signaling pathway-
268 associated genes (*Acvrl1*, *Eng*, and *Id1*), we hypothesized that this pathway responsible for

269 EC quiescence may be inhibited in gCap following lung injury to promote angiogenesis[39].
270 Taken together, these results converge towards pro-angiogenic signaling in *Lrg1*^{pos} PCEC
271 which, by releasing angiocrine factors, could thus contribute to the regeneration of the
272 pulmonary alveolar niche.
273
274 **Bleomycin-induced endothelial remodeling echo pathological signatures found in**
275 **human IPF**
276 Using again the Habermann dataset[34], we then systematically compared the mouse fibrotic
277 signature induced by bleomycin with the IPF signature in systemic EC, PV EC, gCap, and
278 aCap (**Fig. 3H and Supplementary table S6**). The most conserved pathological signature in
279 both models was found for systemic EC, with a common modulation of 218 genes that includes
280 most of the pro-angiogenic signature enriched in mouse *Lrg1*^{pos} PCEC (**Table 2**). Moreover,
281 we observed a conserved upregulation of several signaling-associated genes, transcription
282 factors and ECM-associated genes. With regard to conserved downregulated genes, we also
283 observed a common inhibition of multiple transcription factors, including FOXF1, SMAD6 and
284 GATA2 as documented recently[40] as well as genes -associated with signaling, notably the
285 BMP9 signaling genes (**Table 2**). These findings show that the pulmonary endothelial
286 remodeling observed after bleomycin-induced lung injury in mice mimics at least in part the
287 recruitment of systemic EC occurring in IPF, with a conserved signature associated with
288 angiogenesis, ECM organization and cell adhesion.
289
290 ***Lrg1*^{pos} PCEC dynamics are delayed in fibrotic aged mouse lungs.**
291 We then compared the dynamics of pulmonary EC after injury and during resolution between
292 young and old mice (**Fig. 4A**), leveraging on their relative proportions found in each mice of
293 the Chromium scRNA-seq dataset. The proportion of sCap, which were weakly detected in the
294 control lungs, increased after bleomycin instillation and progressed during the resolution
295 phase, suggesting that their recruitment is sustained over time independently of aging, even
296 though the emergence of these cells appears to be more prominent in young mice at the peak
297 of fibrosis. The presence of Col15a1^{pos} cells was confirmed by RNAscope^{TM} FISH in lungs from
298 both BLM-challenged young and aged mice, from the peak of fibrosis up to D60 **(Fig. 4B**). We
299 observed a similar profile between *Lrg1*^{pos} gCap and *Lrg1*^{pos} aCap, which sharply increased at
300 d14 post bleomycin instillation and then diminishes upon resolution in young mice, while these
301 increases were weaker and rather peaked at D28 in old animals. The simultaneous detection
302 of Prolif. EC and conservation of the pool of physiological gCap and aCap supported that lung
303 injury induces neovascularization of capillary EC. However, this regenerative response was
304 stronger and shorter in young animals and also affected venous vessels.

305 We confirmed these observations at the gene-level by calculating a score based on the
306 expression of upregulated genes following bleomycin-induced lung injury, which we compared
307 between cells grouped by age and time point (**Fig. 4C** and **Supplemental Fig. S6A-D**).
308
309 We also validated this delayed dynamic in an independent cohort of mice using *in situ*
310 hybridization assay, showing that in young mice, *Lrg1*^{pos} cells peaked at day 14 following
311 bleomycin treatment and progressively decreased to reach their basal level at day 60, whereas
312 a strong percentage was still maintained at day 28 and day 60 in old mice. Similarly, we
313 observed the same evolution pattern with *Lrg1*^{pos} *Aplnr*^{pos} cells and *Lrg1*^{pos} *Ednrb*^{pos} cells,
314 corresponding to *Lrg1*^{pos} gCap and *Lrg1*^{pos} aCap, respectively (**Fig. 4D**).
315 Finally, we returned to the spatial transcriptomic data to look for evidence of physiological and
316 pathological PCEC signatures in spatial topics potentially associated with Lrg1 expression.
317 Topic 6, highly represented in the young lung section at d28, was enriched in physiological
318 gCap and aCap markers (*Sema3c, Hpgd, Thbd, Cldn5*, and *Car4*), as well as AT1 markers
319 (*Ager, Hopx, Cldn18*), suggesting successful restoration of alveolar functions (**Fig. 1F,**
320 **Supplemental Fig. S1B-C**). *Lrg1* was found in topics 1 and 4, where it was associated with
321 fibroblast markers rather than endothelial markers. Interestingly, it was also enriched in topic
322 13, which displayed a clear inflammatory signature (**Fig. 1E**), notably carried by cytokines,
323 complement and MHC components. This topic persisted at D28 in both lung sections from old
324 mice (representing 6% and 10% of deconvoluted spots respectively), whereas it tended to be
325 cleared (2% of deconvoluted spots) in the section from young mice at the same time point.
326 Taken together, our results showed that the dynamics of Lrg1^{pos} PCEC cells are delayed in
327 lungs from aged mice, paralleling the retarded resolution of lung fibrosis observed in aged
328 animals.
329
330 **Aged mouse lung gCap exhibit pro-inflammatory and injury-activated phenotype**
331 We next performed differential expression analyses between old and young gCap in fibrotic or
332 control conditions. In fibrotic conditions, we observed an enriched pro-inflammatory signature
333 in old gCap, mainly characterized by the overexpression of genes encoding for MHC class II
334 molecules, *Cd74*, *Cd52* and the interferon-induced protein Gbp4 (**Fig. 5A-B and**
335 **Supplementary table S4**). The expression of *Cd74*, the receptor of Macrophage migration
336 Inhibitory Factor (MIF), a critical upstream regulator of the immune response[41] was validated
337 by RNAScope™ ISH, showing a stronger signal of *Cd74* in lungs from BLM-treated aged mice
338 as well as partial co-localization of *Cd74* and *Lrg1* (**Fig. 5C**). Conversely, we found in young
339 gCap an enrichment of transcription factors associated with vascular homeostasis and repair
340 such as *Klf2, Klf10 and Peg3*[42-44] (**Fig. 5B and Supplementary table S4**). In PBS-treated
341 mice, comparison between old and young gCap revealed even more gene modulations (**Fig.**

342 **5D-E**), which were associated with multiple functions, including an increase of inflammatory
343 and immune responses, but also ECM organization and IPF signaling pathway in aged mice
344 (**Fig. 5F and Supplementary table S5**). Indeed, this aging signature contained 21 genes
345 significantly deregulated in gCap following bleomycin challenge, including the top *Lrg1*^{pos}
346 PCEC markers *Lrg1*, *Col15a1*, *Nrtk2*, *Ndrg1* and *Ankrd37* (**Fig. 5G)**, indicating that old gCap
347 in physiological condition already express a pro-inflammatory and injury-activated signature.
348 We also observed that old gCap overexpressed *Vwf*, *Slc6a2*, *Prss23 and Plat* (**Fig. 5D-E**),
349 which are normally restricted to macrovascular EC **(Supplemental Fig. S3A).** These cells also
350 show a decrease in *Aplnr* expression compared to young gCap, in line with a predicted
351 decrease in the Apelin signaling pathway in old gCap (**Fig. 5F**), strongly suggesting a potential
352 change in their intrinsic functions.
353
354 **Trajectory inference indicates a transition between *Col15a1*^{pos} sCap, *Lrg1*^{pos} gCap and**
355 **physiological gCap following alveolar injury.**
356 The parallel kinetic profile between the *Lrg1*^{pos} PCECs populations after BLM treatment as well
357 as their transcriptomic proximity and delayed appearance in aged animals, correlating with a
358 delayed resolution, suggest that a dynamic process links these different PCEC subpopulations
359 or cell states during alveolar niche regeneration. To model a potential trajectory in an unbiased
360 way, we used the generalized RNA velocity approach[45], leveraging on the splicing dynamics
361 estimated in young bleomycin and PBS-treated mice samples at day 14. Latent time ordering
362 indicated that *Col15a1*^{pos} sCap could initiate a differentiation process, transiting through *Lrg1*^{pos}
363 gCap before ending up to physiological gCap **(Fig. 6A)**. Of note, the same trajectory was
364 proposed in the same configuration in the old mice 28 days after instillation (**Fig. 6B)**. This
365 inferred trajectory was supported by genes displaying a dynamic expression profile according
366 to latent time, either progressively decreasing (*Smad1, Sparc, Col4a1, Ndrg1, Igfbp7*),
367 transiently upregulated (*Ackr3, Emp1, Cmah, Vwf, Smad7*), or progressively increasing (*Npr3*,
368 *Hpgd*, *Clec1a*, *Bmp6*, *Itga1*) (**Fig. 6C-D and Supplemental Fig. S7A)**. These data suggest
369 that in the bleomycin reversible fibrosis model, sCap are recruited to contribute to gCap
370 replenishment and to the regeneration of the lung capillary endothelium integrity
371 (**Supplemental Fig. S7B).**
372
373 **DISCUSSION**
374 In this work, we used scRNA-seq combined with spatial transcriptomics to follow the
375 transcriptomic modifications of lung cell populations during fibrosis formation and resolution in
376 a mouse model of lung fibrosis. We specifically focused on the transcriptomic alterations
377 correlated with a delayed fibrosis resolution in aged mice and identified several aging-
378 associated changes in some PCEC subpopulations, including aCap and gCap, shifting towards

379 a pro-angiogenic phenotype expressing *Lrg1* and associated with alveolar niche regeneration.
380 We also found that aging altered the transcriptome of gCap in control mice, with a signature
381 suggestive of a pro-fibrotic and injury-activated state. Because PCEC are intimately connected
382 to alveolar epithelial cells and fibroblasts in the alveolus, age-associated defects in the PCEC
383 differentiation may likely participate in the dysfunction of other cells in the alveolar niche and
384 impede alveolar regeneration.
385 Our study presents a whole picture of cell dynamic changes in lung from young and aged
386 animals during fibrosis formation and resolution at 3 time points. Using several approaches,
387 we confirmed previous works showing that aged mice exhibit impaired resolution after
388 bleomycin injury[23-25], further proposing using spatial transcriptomics that infiltration of immune
389 cells such as plasma cells, known in IPF to form aggregates and bronchus-associated
390 lymphoid tissue (BALT)[29], contribute to this delayed resolution in aged mice. We also confirmed
391 by scRNA-seq that many cell populations are affected by bleomycin, including AEC,
392 fibroblasts, macrophages and PCEC[26, 32, 33, 46], providing a useful dataset to analyze the
393 transcriptomic dynamic of these populations and compared it to the kinetic of the resolution
394 process measured with histology, collagen production and spatial transcriptomic.
395 One of the most affected cell type by the bleomycin challenge in our dataset corresponded to
396 EC, with several main subpopulations that were only apparent in bleomycin-injured lungs. First,
397 we identified a homologous Col15a1-positive systemic EC population, previously described in
398 lungs from IPF patients[13]. We also found that this population, described originally as being of
399 venous macrovascular origin, doesn't express clear macrovascular and venous markers and
400 likely corresponded to a systemic capillary ECs (sCap) in agreement with a recent study in
401 COVID-19 patients[15]. Secondly, we found two new subpopulations of gCap and aCap cells in
402 fibrotic lungs sharing a partial common gene signature characterized by the overexpression of
403 *Lrg1*. Interestingly, among these distinct populations, only *Lrg1*^{pos} gCap and *Lrg1*^{pos} aCap cells
404 displayed a different kinetic profile following bleomycin challenge in young and aged mice.
405 While they both peaked at day 14 in young mice lungs, their dynamic was strongly shifted in
406 the lungs of aged mice, peaking at day 28. Overall, our findings demonstrate that bleomycin
407 injury induces PCEC remodeling marked by the upregulation of *Lrg1* and the emergence of
408 distinct capillary activated cell states that are delayed in aged mice.
409 *Lrg1* codes for a secreted member of the family of leucine-rich repeat proteins, that often
410 served as pattern recognition motifs for the innate immune system[47]. It is a multifunctional
411 signaling molecule initially associated with pathological angiogenesis[36] that can notably
412 modulate the TGF-β pathway in a highly context-dependent manner. The physiological
413 function of *Lrg1* remains poorly understood, with knockout mice showing no obvious
414 phenotypic defects. Several studies indicate that it promotes physiological wound healing and
415 maintain tissue homeostasis[48, 49], although abnormal expression levels has been found to

disturb effective would healing and contribute to fibrosis in several tissues including lung[50]. These data suggest that *Lrg1* expression must be finely regulated during the repair process and that abnormal levels may disrupt effective wound healing and contribute to fibrogenesis. One of the most compelling examples of LRG1 function in promoting diseased vessels is commonly described as the "TGF-β angiogenic switch", which switches TGF-β signaling to a proliferative pathway in a variety of pathological settings, including age-related macular degeneration and cancer[36]. While binding of TGF-β to endothelial TGF-β type II receptor (TGFβRII) normally initiates signaling through the tyrosine kinase receptor ALK5 coupled to SMAD2/3, preserving cell quiescence, high levels of LRG1 can redirect TGF-β to form a transduction complex with ALK1 and the accessory receptor endoglin (ENG), activating the pro-angiogenic SMAD1/5/8 pathway and promoting EC proliferation, migration and tubulogenesis as well as the expression of several pro-angiogenic factors such as VEGFA. Our in vitro experiments confirmed this molecular mechanism, which likely explains our data showing inhibition of endothelial quiescence in gCap *Lrg1*^{pos} as well as strong induction of markers associated with EC proliferation and migration after lung injury to promote angiogenesis and sprouting. During the preparation of this manuscript, Zhao et al. indeed demonstrated that *Lrg1* was able to counterbalance the canonical angiostatic TGFβRII signaling to promote lung vascular repair following viral injury[51]. While this *Lrg1*-associated pro-angiogenic activity appears to be necessary to promote alveolar vascular repair, it is likely that delayed expression of *Lrg1* in aged mice could slow down the formation of a new mature capillary network thus causing a delay in the regeneration of the alveolar niche.

The *Lrg1*-associated gene signature found in our study also contains *Sox17*, a member of the Sry-related high mobility group domain family F (Sox F) transcription factors, a key developmental regulator of EC lineage. Previous work indicated that induction of *Sox17* expression through the activation of HIF-1α in EC plays an essential role in regenerating EC following endotoxin-induced EC injury, notably by transcribing Cyclin E1 and stimulating proliferation of EC[52]. Of note, both *SOX17* and *HIF1A* were also detected in PCEC in lungs from IPF patients, indicative of a pro-angiogenic activity. Overexpression of these two genes were validated in fibrotic areas of lung mice, with co-localization with *Aplnr* or *Lrg1*, respectively. The activation of a hypoxic response was also particularly visible in *Lrg1*^{pos} aCap and *Lrg1*^{pos} gCap with several markers associated with glycolysis and hypoxia, in agreement with studies indicating that transient activation of hypoxia-mediated signaling pathways contributed to angiogenesis and vascular repair[53]. In addition to hypoxia, our analysis revealed transcriptomic modulations of mTOR, TGF-β, IL-8 and integrin-linked kinase signaling and related notably to vasculogenesis, sprouting, cell-cell contact, cell migration and inflammation. The identification of multiple cytokines/growth factors and receptors in activated PCEC suggested extensive heterotypic interactions within the alveolar niche. Our ligand-receptor

interaction predictions propose a complex network of interactions involving ligands expressed by activated PCEC and neighboring cell types within the alveolar niche, including AT1, AT2, mesenchymal cells as well as mast cells, neutrophils and macrophages that likely influence alveolar repair. Remarkably, some of these predictions are in agreement with previous studies highlighting in particular the importance of the signaling pathway involving *Cxcl12* (also known as SDF-1) and *Ackr3* (*Cxrc7*) in PCEC, leading to neo-alveolarization[38]. Further work is needed to analyze the functional importance of this predicted network and to characterize their central regulators with the goal to potentially target specific signaling pathways within the vascular niche for regenerative therapies.

We also found additional aging-related transcriptomic differences in PCEC subpopulations in physiological or pathological conditions. We focused on gCap population that functions as progenitor cell for aCap in capillary homeostasis and repair[9]. We found that in lungs from aged bleomycin-challenged mice, gCap expressed an enriched pro-inflammatory and immune signature, as well as decreased expression levels of several transcription factors associated with vascular homeostasis, repair and the anti-inflammatory response (*Klf2, Peg3, Klf10)*[42-44], indicating that the bleomycin response was exacerbated in gCap from aged mice. In addition, we also found an aging-related signature in gCap from healthy control lungs. Part of this signature (21 genes), corresponding mostly to genes associated with angiogenesis, migration and sprouting, was correlated with the bleomycin-induced signature, suggesting a pre-inflammatory and injury-activated cell state in old gCap.

Our study has limitations, in particular because of some technical biases during the single-cell and spatial transcriptomic workflow. First, our dissociation protocol, combined with the cell Hashing protocol[30], requiring additional cell labeling and washes has led to a depletion of fibroblasts and epithelial cells, which did not allow us to perform a complete cell state analysis for these cell types. Secondly, while the Visium spatial technology skips the dissociation step, its resolution did not allow to perform a single-cell characterization of the multiple cell lineages composing the alveolar niche, despite the use of a deconvolution tool. Moreover, although this approach was intended to highlight some spatial information explaining the resolution delay in aged mice, it will need to be supplemented by a larger number of replicates to improve these observations. Finally, the bleomycin mouse model may not accurately recapitulate the vascular alterations observed in IPF patients. The comparison of our data with a public dataset from the IPF cell atlas[34] indicated that *LRG1* transcript was expressed at a low level in *COL15A1*^{pos} systemic EC, questioning the relevance of this mouse model. Nevertheless, several conclusions could be drawn from this analysis, including a large conserved pathological signature of 218 genes between the *Col15a1*^{pos} sCap from fibrotic mouse and IPF lungs, confirming their close functional state and a common pro-angiogenic signature between PCECs from mouse fibrotic lungs and human IPF systemic EC, suggesting that the pulmonary

490 endothelial remodeling observed after bleomycin-induced lung injury in mice mimics the
491 recruitment of systemic EC occurring in IPF. In contrast, the aCap *Lrg1*^{pos} and gCap *Lrg1*^{pos}
492 populations were not clearly detected in IPF samples and only a small fraction of genes
493 appeared to be commonly modulated in aCap/gCap populations from fibrotic lungs in humans
494 and mice. The characterization of EC heterogeneity in IPF is still in its infancy. In particular, it
495 is not known whether the ectopic presence of *COL15A1*^{pos} systemic EC in the IPF-associated
496 distal parenchyma, play a role in the pathogenesis of IPF. In order to gain information on their
497 potential function, we used our scRNA-seq dataset on young PCEC at day 14 to investigate
498 the potential relationship between sCap and gCap using the RNA velocity approach[45]. Our
499 results indicate that following lung injury, sCap are recruited and may function as progenitor
500 cells that can initiate a differentiation process, transiting through Lrg1^{pos} gCap before reaching
501 the physiological gCap cell state. The same differentiation scheme was also found in the old
502 mice but with a delayed kinetic (28 days). Overall, these data suggest that in a reversible
503 fibrosis model (mouse), sCap are recruited and can act as progenitor cells to reconstitute the
504 gCap pool and regenerate the integrity of the alveolar endothelial capillaries while aging
505 appears to delay this resolution process. It is therefore tempting to hypothesize that in the
506 context of the human pathology, systemic EC might be deficient in this differentiation process
507 and accumulate in the injured tissue. Interestingly, a recent article, using an *ex vivo* human
508 precision-cut lung slice (hPCLS) model of lung fibrogenesis, also described a transcriptomic
509 proximity between alveolar PCEC and a systemic venous EC state[54]. In this case, the authors
510 presented a differentiation trajectory in the opposite direction, proposing that PCEC in injured
511 alveoli give rise to a *VWA1*^{pos}/*PLVAP*^{pos} ectopic EC state with transcriptional similarities to the
512 systemic vasculature. Additional analyses are thus needed to better characterize this ectopic
513 EC state versus the *COL15A1*^{pos} systemic EC and distinguish between these two hypotheses.
514 During the revision of this manuscript, a study by Raslan et al. also investigated the bleomycin-
515 induced lung injury response in young and aged mice at single-cell resolution[55]. Interestingly,
516 they also isolated a sub-population of gCap EC marked by the expression of *Ntrk2/TrkB*
517 (Tropomyosin Receptor Kinase B) that appeared in bleomycin-injured lungs and associated
518 with aberrant YAP/TAZ signaling, mitochondrial dysfunction, and hypoxia. These cells
519 exhibited a similar gene expression signature as those we present here, including the
520 upregulation of *Lrg1*. However, their conclusions, stating that this population is dysfunctional
521 and accumulates with aging, differ from ours. One explanation for this discrepancy could be
522 that they studied only a single time point (day 30), without considering the dynamic of
523 appearance and disappearance of this population at earlier and later times. Further functional
524 investigations aimed at depleting these *Lrg1*^{pos} sub-populations *in vivo* will be required in order
525 to clarify these two contrasting hypotheses.

526 Altogether, our findings shed new light into the molecular mechanisms associated with alveolar
527 endothelial capillaries resolution in a mouse model of reversible lung fibrosis and how aging
528 influences specific PCEC to delay this resolution process. In particular, they raise new
529 hypotheses regarding the functional importance of these specific PCEC populations in lung
530 repair, which may lead to new therapeutic strategies for the treatment of IPF.
531

532 **METHODS**

533

534 **Reagents and antibodies**

535 Bleomycin was obtained from Sigma Aldrich (B1141000). The following antibodies were used
536 in immunofluorescence experiments: Mouse Anti-Human CD31 (MA5-13188 Thermofisher),
537 Rabbit Anti-Human COL15A1 (53667 Invitrogen), Purified Mouse Anti- αSMA–FITC (F3777
538 Sigma-Aldrich), donkey DyLight 594 Anti-Rabbit IgG (A32754 Life Technologies), donkey
539 DyLight 647 Anti-Mouse IgG (A31571 Life Technologies). The following antibodies were used
540 in western blot experiments: Rabbit anti-Human pSmad2 (18338, Cell signaling), Rabbit anti-
541 Human Smad2 (5339, Cell signaling), Rabbit anti-Human pSmad1/5 (9516, Cell
542 signaling),Rabbit anti-Human Smad5 (9517, Cell signaling), Rabbit anti-Human LRG1 (PA5-
543 96832, Thermofisher), Rabbit anti-Human HSP90 (4877, Cell signaling) and Goat anti-rabbit
544 HRP (P0448, Dako).

545

546 **Experimental design and animal treatment.**

547 All animal care and experimental protocols were conducted according to European, national
548 and institutional regulations (Protocol numbers: 00236.03 and APAFIS#31298, IPMC approval
549 E0615252; Protocol Number APAFIS#12540, University of Lille; approval 00236.03 CNRS).
550 Personnel from the laboratory performed all experimental protocols under strict guidelines to
551 ensure careful and consistent handling of the mice. Seven-week ("young") and 18-month
552 ("old")-old C57BL/6 male mice (Charles River) were divided randomly into two groups: (A)
553 saline-only (PBS, n=3), or (B) bleomycin (BLM, n=3). To induce fibrotic changes, 50-µl
554 bleomycin (1 U/kg) or PBS was aerosolized in mouse lungs using a MicroSprayer Aerosolizer
555 (Penn-Century, Inc.) as previously described [56]. Mice were sacrificed at designated time points
556 (days 14, 28 and 60) after instillation.

557

558 **IPF lung tissue sections.**

559 Lung tissue sections were obtained from the UGMLC Giessen Biobank affiliated to the
560 European IPF Registry as well as from the Nice Hospital-Integrated Biobank (transfer
561 authorization from the French ministry of research n° AC-2021-4655).

562

563 **Histopathology.**

564 Lungs were fixed overnight with neutral buffered formalin and then embedded in paraffin. 5-
565 micrometer-thick sections were mounted and stained with hematoxylin and eosin (HE) as well
566 as Sirius Red to assess the degree of fibrosis. HE sections were scanned using Axio Scan Z1
567 scanner (Zeiss) at x10 magnification. Data are processed using the Zen blue imaging software

568 (Zeiss). Hematoxylin and eosin zoomed in pictures were performed using Axiophot 2 light
569 microscope.
570
571 **Hydroxyproline quantification of mouse lungs.**
572 Lung hydroxyproline content was assayed as previously described [56]. Briefly, lungs were
573 disrupted in liquid nitrogen and 10 mg were homogenized in 100 µl of water. Samples were
574 hydrolysed for 3 hours at 120°C in a temperature-controlled heating block after adding 100 µl
575 of HCl 12M and then dried. Hydroxyproline quantification was finally performed in microplate
576 as described by the manufacturer (Sigma).
577
578 **Visium™ spatial transcriptomics protocol**
579 ***Tissue preparation.*** Tissue preparation and slides processing were performed according to
580 the Visium Tissue Preparation Guide (CG000238 Rev A; CG000239 Rev A; CG000240 Rev
581 A, 10× Genomics). Briefly, lungs of bleomycin-challenged mice (Young.D14/D28;
582 Old.D14/D28, n=2 for a total of 8 samples) were inflated with diluted Optimal Cutting
583 Temperature (OCT), gently removed from mice and then embedded in OCT on dry ice and
584 stored at -80°C. OCT blocks were cryosectioned at 10µm thickness on capture areas of Visium
585 10 Genomics slide. Before performing the complete protocol, Visium Spatial Tissue
586 Optimization was performed according to manufacturer's procedure and using the Axioscan 7
587 scanner (Zeiss). Thirty minutes was selected as optimal permeabilization time. The
588 experimental samples were fixed, stained with H&E and imaged using Axioscan 7 scanner at
589 5x magnification.
590 ***Generation of spatial transcriptomic libraries.*** Library preparation was performed according
591 to the Visium Spatial Gene Expression User Guide. Libraries were loaded and sequenced on
592 a NextSeq2000 System (Illumina) as paired-end-dual-indexed, at a sequencing depth of
593 approximately 25 M read-pairs per capture area.
594 ***Analysis of spatial transcriptomics data.*** The 8 space ranger pipeline outputs containing
595 both the spot-level gene counts and the histological image of the tissue slice were read as
596 seurat objects. After a quick overview of each one, 2 of them (Young.D14_#2 and
597 Young.D28_#2) appeared unusable because of a very low level of detected molecules per
598 spot (<800 detected genes). The remaining 6 samples (Young.D14, Old.D14.a, Old.D14.b,
599 Young.D28, Old.D28.a, Old.D28.b) were jointly processed using the SpatialExperiment[57]
600 (v1.10.0) and STDeconvolve[27] (v1.3.1) R packages. Firstly, the genes x spots count matrices
601 of the 6 samples were stripped of mitochondrial, ribosomal, unannotated non-coding and
602 hemoglobin subunit coding genes. The preprocess() function was run a first time on each
603 sample to identify overdispersed genes, using the following arguments: nTopGenes = 5,
604 removeAbove = 0.95, min.reads = 10, min.lib.size = 1, min.detected = 1, ODgenes = TRUE,

605 od.genes.alpha = 0.05, gam.k = 5, nTopOD = 1000. We took the union of the 6 lists of
606 overdispersed genes, representing 2482 unique genes. The preprocess() function was run a
607 second time on the concatenated count matrix of those 2482 genes in all spots, specifying to
608 discard spots containing less than 200 UMIs, and genes detected in less than 10 spots,
609 resulting in a corpus of 2479 genes x 10813 spots count matrix and the associated spatial
610 coordinates. The fitLDA() function was run on the count matrix in order to help selecting an
611 optimal number K of predicted topics. Following the recommendations of the authors, we chose
612 a value of K=14, i.e. the value that produces the smallest perplexity without exceeding 5 topics
613 with an average proportion of less than 5%. The topics proportions across spots (theta) and
614 topics gene probabilities (beta) matrices from the optimal fitted LDA model were obtained with
615 the getBetaTheta() function with a betaScale factor = 1000 to scale the predicted topics gene
616 expression profiles. To annotate each of the 14 topics, the log2FC of all expressed genes were
617 calculated by dividing the expression in the topic versus the average expression in the rest of
618 the topics. Genes with a log2FC > 0.4 were used to perform a canonical pathway enrichment
619 in each topic using Ingenuity Pathway Analysis (Ingenuity® Systems, www.ingenuity.com).
620
621 **Chromium™ single-cell transcriptomics protocol**
622 ***Lung dissociation and cell preparation.*** Lung single cell suspensions were generated as
623 previously described[58]. Briefly, after euthanasia, lung tissue was perfused with sterile saline
624 through the heart and were inflated through the trachea with dissociation cocktail containing
625 dispase (50 caseinolytic U/ml), collagenase A (2 mg/ml), elastase (1 mg/ml), and DNase (30
626 µg/ml). Lungs were immediately removed, minced to small pieces ~1mm3), and transferred for
627 mild enzymatic digestion for 20–30 min at 37 °C in 4 ml of the dissociation cocktail. Enzymatic
628 activity was inhibited by adding 5 mL of PBS supplemented with 10% fetal calf serum (FCS).
629 Single cells suspensions were passed through a 40-micron mesh, and then harvested by
630 centrifugation at 300 g for 5 min (4°C). Reb blood cell lysis was performed using RBC lysis
631 buffer (Thermo fisher) for 2 min at 4°C and stopped using PBS 10% FCS. After another
632 centrifugation at 300g for 5 min (4°C) cells were counted and critically assessed for single cell
633 separation and overall cell viability using the Countess 3 FL (Fisher Scientific). Samples were
634 then stained for multiplexing using cell hashing [3], using the Cell Hashing Total-Seq-ATM
635 protocol (Biolegend) following the protocol provided by the supplier, using 6 distinct Hash Tag
636 Oligonucleotides-conjugated mAbs (3 PBS and 3 Bleo). Briefly 1.10^6 cells were resuspended
637 in 100µl of PBS, 2% BSA, 0.01% Tween and incubated with 10µl Fc Blocking reagent for 10
638 min 4°C then stained with 0.5µg of cell hashing antibody for 20 minutes at 4°C. After washing
639 with PBS, 2% BSA, 0.01% Tween samples were counted and merged at the same proportion,
640 spun 5 minutes 350 x g at 4°C, resuspended in PBS supplemented with 0.04% of bovine serum

641 albumin at final concentration of 500 cells/µl and pooled sample were immediately loaded on
642 Chromium.
643 ***Generation of single cell librairies, 10X Genomics scRNA-seq and data processing.***
644 Single-cell capture was performed using the 10X Genomics Chromium device (3′ V3). Single-
645 cell libraries were sequenced on the Illumina NextSeq 500. Alignment of reads from the single
646 cell RNA-seq libraries and unique molecular identifiers (UMIs) counting were performed with
647 10X Genomics Cell Ranger tool (v3.0.2). Reads of oligonucleotides tags (HTOs) used for Cell
648 Hashing were counted with CITE-seq-Count (v1.4.2). Counts matrices of total RNA and HTOs
649 were thus obtained for the 6 sequencing run, respectively named YoungD14, YoungD28,
650 YoungD60, OldD14, OldD28 and OldD60.
651 ***Single cell data secondary analysis.*** All downstream analyses were carried out with Seurat
652 R package (v4.1.0).
653 *HTOs demultiplexing.* For each 6 sequencing run, RNA and HTOs counts matrices were
654 integrated into a Seurat object. HTOs counts were demultiplexed with HTODemux function to
655 assign mice-of-origin for each cell (3 PBS-treated and 3 Bleomycin-treated). Only the cells
656 identified as “Singlet” and passing quality control metrics (more than 200 detected genes, less
657 than 0.25% of mitochondrial content) were kept for each Seurat object. The 6 seurat objects
658 containing the raw counts of filtered cells and their metadata (age, day of lung collection post
659 injection, treatment, mice-of-origin) were merged.
660 *Samples integration.* The computational integration of the different samples was performed
661 using reciprocal PCA, as described in the dedicated vignette from Satija lab website
662 (https://satijalab.org/seurat/articles/integration_rpca.html). Briefly, a “detailed samples”
663 metadata column was created by aggregating age, day of lung collection post injection and
664 treatment (ex: Young.D14.Bleo, Young.D14.PBS, etc). According to this “detailed samples”
665 metadata, cells were split into 12 seurat objects. For each of 12 datasets, raw counts were
666 normalized using SCTransform with Gamma-Poisson generalized linear model to estimate
667 regression parameters. 3000 features were selected for being repeatedly variable across the
668 12 datasets. The sctransform residuals corresponding to the selected 3000 features were
669 computed if they were missing in a particular object. Principal Component Analysis (PCA) was
670 run individually for each object on the sctransform normalized counts of the 3000 selected
671 features. A set of common anchors was found among the selected features, in dimensionally
672 reduced data by reciprocal PCA, using FindIntegrationAnchors function with the following
673 arguments: normalization.method = "SCT", dims = 1:50, k.anchor = 5. This set of anchors was
674 used to create a combined object containing integrated data using 50 dimensions for the
675 anchor weighting procedure.
676 *Clustering and annotation.* First, PCA was run on the integrated data. UMAP and kNN
677 clustering were computed on the first 80 computed principal components (PCs). Clusters

678 corresponding to aggregates of cells sharing a low-UMIs content were discarded. The entire
679 integration and clustering processes were rerun on the cleared dataset, following the exact
680 steps described above. The finally obtained clusters were annotated on the basis of the
681 expression of their specific markers listed in the output of the FindAllMarkers function. Cell
682 type–specific marker genes were established using the Wilcoxon rank sum test with P values
683 adjusted for multiple comparisons using the Bonferroni method. Adjusted P values <0.05 were
684 considered significant.
685 *Differential expression analyses* between fibrotic and PBS conditions in all cell populations.
686 Differential expression analyses between cells from bleomycin and PBS treated mice were
687 carried out with DESeq2. First, all counts of each cell population from the same mice were
688 aggregated to create a pseudobulk sample. For the PBS condition, we thus systematically
689 obtain 18 pseudobulks samples corresponding to the 3 young and 3 old PBS-treated lungs
690 collected at day 14, at day 28 and at day 60. For the fibrotic condition, we excluded the samples
691 from bleomycin-treated lungs collected at day 60, which correspond to an almost complete
692 fibrosis resolution. We thus obtained 12 pseudobulks corresponding to the 3 young and 3 old
693 bleomycin-treated lungs collected at day 14 and at day 28. For the alveolar macrophages
694 pseudobulks, all counts from the 3 subpopulations (AM1, AM2, AM3) were aggregated. For
695 gCap and aCap pseudobulks, all counts of gCap plus Lrg1^{pos} gCap or aCap plus Lrg1^{pos} aCap
696 were aggregated. Genes considered as differentially expressed were selected according to an
697 adjusted p-value threshold of 0.05, obtained with the Wald test and the Benjamini-Hochberg
698 method for multiple tests correction implemented in DESeq2.
699 ***Detailed analysis of endothelial cells (EC).***
700 *Identification of EC subpopulations.* The clusters corresponding to general capillary cells
701 (gCap) and aerocytes (aCap) were extracted and subclustered using the 80 PCs already
702 computed from the integrated assay of the complete dataset. Clusters corresponding to Lrg1^{pos}
703 aCap, Lrg1^{pos} gCap and sCap subpopulations were added to the annotation and UMAP was
704 rerun on the subset of cells corresponding to gCap, aCap, proliferating EC, Lrg1^{pos} aCap,
705 Lrg1^{pos} gCap, sCap, PV EC and Arterial EC using the same number of dimensions. The original
706 raw counts were finally log-normalized with NormalizeData for all data exploration and
707 visualization.
708 *Relative subpopulations frequencies.* All PBS-treated mice with the same age and sacrificed
709 at D14, D28 or D60 were considered as replicates (n=9), while Bleomycin-treated mice were
710 separated according to age and time of sacrifice (n=3 for each time point). The relative
711 subpopulations frequencies at the 4 time points (PBS, D14, D28, D60) were obtained by
712 calculating the ratio between the number of cells in each subpopulation and the total number
713 of cells in each mouse replicate, either mixing or distinguishing young and old mice. Differential
714 abundance analyses were carried out using edgeR (v3.32.1) to model overdispersed numbers

715 of cells per group with the NB GLM method and then to test for differences in abundance
716 between sample groups with the glmQLFTest function, which performs empirical Bayes quasi-
717 likelihood F-tests and FDR controlling.
718 *Bleomycin-induced fibrosis score.* To compute a bleomycin-induced fibrosis score in gCap,
719 aCap and PVEC, only the most significant upregulated genes from the differential expression
720 analyses described above were selected according to adjusted p-value (<0.05),
721 log2FoldChange (>0.5) and base mean expression (>10 for gCap, >5 for aCap and PV EC).
722 Lists of selected genes were used to compute a score at the single cell level using the
723 AddModuleScore function. Scores were finally compared between the 4 time points (PBS,
724 D14, D28, D60) and between young or old animals, using the Wilcoxon rank sum test
725 implemented in the FindMarker function.
726 *Comparison between old vs young gCap in fibrotic and physiological conditions.* To compare
727 the transcriptomic profiles of gCap from old and young mice in fibrotic condition, counts from
728 bleomycin-treated gCap and Lrg1^{pos}gCap were aggregated within the same mouse for day 14
729 and day 28 time points, in order to obtain 6 young and 6 old pseudobulks samples. The same
730 process has been applied to build pseudobulk samples of physiological gCap but including day
731 60 samples, resulting in 9 pseudobulks for either young of old groups. Differential analysis
732 between old and young pseudobulks samples were carried out with DESeq2. DEGs were
733 selected according to adjusted p-value (<0.05), absolute log2FoldChange (>0.5) and base
734 mean expression (>5).
735 *Systemic EC transcriptomic signature in fibrotic condition.* As systemic EC from control
736 samples were poorly detected either in mouse or human data, systemic EC from fibrotic
737 conditions were compared to control systemic EC plus control PV EC using the pseudobulk-
738 based approach.
739 *Ingenuity Pathway Analysis.* To investigate the enriched pathways and functions associated
740 to DEGs either in the fibrotic versus control comparison or old versus young comparison, we
741 used the core analysis of the Ingenuity Pathway Analysis tool (Ingenuity® Systems,
742 www.ingenuity.com) using the results of the treatment (bleomycin)- or aging-perturbed genes
743 obtained by DGE testing (see above) as input.
744 ***RNA velocity analyses.*** The RNA velocity analyses were carried out following the kallisto |
745 bus (https://bustools.github.io/BUS_notebooks_R/velocity.html) and scVelo workflows
746 (https://scvelo.readthedocs.io/).
747 *Generation of spliced and unspliced matrices.* Intronic sequences of the mouse genome
748 assembly GRCm38 were first identified using the get_velocity_files function of the BUSpaRse
749 R package (v1.5.2) and the gencode annotation (v.M25). In order to allow the pseudoalignment
750 of reads on both cDNA and identified intronic sequences, indexes for both cDNA and intronic
751 sequences were built using kallisto (v0.46.2). The spliced and unpliced matrices were then

752 generated for each sequencing run using the wrapper combining kallisto and bustools
753 (v0.39.2) functions, typically with the following command line: kb count -i
754 mm_cDNA_introns_index.idx -g tr2g.tsv -x 10xv3 -o kb \
755 -c1 cDNA_tx_to_capture.txt -c2 introns_tx_to_capture.txt --workflow lamanno \
756 sample_x_L001_R1_001.fastq.gz sample_x_L001_R2_001.fastq.gz \
757 sample_x_L002_R1_001.fastq.gz sample_x_L002_R2_001.fastq.gz \
758 sample_x_L003_R1_001.fastq.gz sample_x_L003_R2_001.fastq.gz \
759 sample_x_L004_R1_001.fastq.gz sample_x_L004_R2_001.fastq.gz
760 *Preprocessing.* Generated spliced and unspliced matrices of each sequencing run were then
761 preprocessed to filtered out empty droplets, to remove undetected genes and to replace
762 ensembl IDs by gene symbols. Spliced and unspliced matrices corresponding to barcodes of
763 subset of cells of interest, for example sCap EC, Lrg1^{pos} gCap and gCap from Bleomycin and
764 PBS-treated mice at day 14, were integrated in a seurat object. The spliced raw counts were
765 normalized using SCTransform from seurat R package, and PCA was run on these normalized
766 data, as well as UMAP with the first 30 PCs. The seurat object was then converted to .h5ad
767 file, keeping only the two raw spliced and unspliced assays.
768 *RNA velocity using scVelo.* The .h5ad file was read to an AnnData object using scVelo python
769 package (v0.2.4). Again, data were preprocessed: the counts of the 3000 most variable genes
770 with at list 20 reads were log-normalized using the filter_and_normalize function. PCA and
771 nearest neighbours were computed before the estimation of velocity. The full transcriptional
772 dynamics of splicing kinetics was resolved using the generalized dynamical model and
773 represented as latent time in each cell.
774 ***NicheNet analysis.*** We used the nichenet R package (v1.0.0) [37] to infer ligand-receptor
775 interaction candidates able to induce the expression of pro-angiogenic genes in sCap, Lrg1^{pos}
776 gCap and Lrg1^{pos} aCap cells. For each of these 3 subpopulations, alternatively considered as
777 receiver cells, we computed the activities of ligand sent by all the detected populations of the
778 whole dataset. As genesets, we alternatively used the pro-angiogenic genes expressed in at
779 least one third of cells with an average expression above 1 in the particular subpopulation. For
780 each ligand activities computed for each subpopulation, we selected the top 14 most likely to
781 induce the geneset of interest by ranking them according to Pearson's correlation coefficient.
782 The union of the 3 lists of prioritized ligands resulted in the 17 ligands used for the visualization.
783 The selected receptors of those 17 ligands were only those considered as "*bona fide*", i.e.
784 those whose interaction with their ligand is not only predicted *in silico*. The only exception is
785 for Apoe which didn't have a *bona fide* receptor according to the NicheNet model, for which its
786 best predicted receptor Scarb1 was added. The circos plot linking prioritized ligands and their
787 receptors was realized following the steps described in the dedicated nichenet's vignette
788 (https://github.com/saeyslab/nichenetr/blob/master/vignettes/circos.md).

789 **RNA-FISH.** RNAscope probes against mmu-Lrg1 (ID: 423381), mmu-Aplnr (ID: 436171),mmu-
790 Ednrb (ID: 473801), mmu-Col15a1 (1092391), mmu-Hif1a1 (313821), mmu-Cd74 (437501),
791 mmu-Sox17 (433151), mmu-Vegfa (405131) were prepared and obtained from Advance Cell
792 Diagnostics. FISH assays were performed on FFPE lung sections, as previously described [1]
793 using Multiplex Fluorescent Reagent Kit V2 (Advanced cell Diagnostics) and TSA Plus
794 Cyanine 3 and Cyanine 5 (Perkin Elmer) as fluorophores according to manufacturer's
795 recommendations. Acquisition was performed using an inverted confocal microscope LSM 710
796 (Zeiss) and a 40x oil immersion lens.
797
798 **Immunohistochemistry and Immunofluorescence microscopy.**
799 Five-µm paraffin-embedded sections were deparaffinized/rehydrated and H&E stained as
800 previously described[56]. After washing, the sections were antigen-retrieved using citrate buffer
801 (pH 6.0; Sigma-Aldrich). Autofluorescence was quenched for 20-30 minutes in NH4Cl buffer
802 (0.1M) and passed in Photobleacher for 1h30. Slides were incubated with the primary
803 antibodies (anti-CD31 (1:50), anti-COL15A1 (1:100), Anti-SMA–FITC (1:500)) diluted in a
804 blocking solution BSA (1%) over night at 4°C. After washing in PBS-T (0.05%), slides were
805 incubated for 1h with secondary antibodies (1:400) at room temperature. Nuclei were
806 counterstained with DAPI (1:5000, D1306 Life Technologies). Slides were mounted using
807 Immu-Mount (9990414 Fisher scientific). Representative regions of stained slices were
808 digitalized on an epifluorescent Zeiss microscope and analyzed using the software FIJI.
809
810 **Western blot**
811 Cells were lysed with RIPA cell lysis buffer (Thermofisher) containing phosphatase and
812 protease inhibitors (Invitrogen). Proteins were separated on commercial gradient (4-12%)
813 acrylamide gels and transferred onto PVDF membranes. Proteins were detected by overnight
814 incubation at 4°C with the indicated primary antibodies followed by 1h incubation at room
815 temperature with horseradish peroxidase-coupled secondary antibody and enhanced
816 chemiluminescent substrate (PerkinElmer, Waltham, USA) using a LasImager (GE
817 HealthCare, Chicago, Illinois, USA). Blots were run on parallel gels when proteins of similar
818 molecular weight were analyzed. The western blot quantification was performed with the help
819 of the ImageJ software.
820
821 **Taqman Real time PCR**
822 Total HMEC1 RNA was isolated using trizol (Thermo Fisher Scientific) according to the
823 manufacturer's instructions. RNAs (1 µg) were reverse-transcribed with High capacity cDNA
824 reverse transcription kit (Thermo Fisher Scientific), and PCR was performed using Taqman
825 Real time PCR technology (Applied Biosciences). All reactions were done using Real-Time

826 PCR system (Thermo Fisher Scientific), and expression levels calculated using comparative
827 CT method (2 DDCT). Gene expression levels were normalized to RPLP0 level. The following
828 probes from Taqman (Applied Bioscience) were used: Hs-RPLP0 (99999902-m1), Hs-VEGFA
829 (00900055-m1) and Hs-SMAD2 (00183425-m1).
830
831 **Re-analysis of public scRNA-seq datasets.**
832 Human lung fibrosis [34] and mouse lung public datasets [35] were re-analyzed using reciprocal
833 PCA, in order to integrate samples from different patients or different mice. To reduce the
834 complexity of the human lung fibrosis dataset, we only kept cells coming from either IPF-
835 diagnosed or normal samples and we randomly sampled 10000 immune cells and 5000
836 epithelial cells to reduce the dataset dimensionality. Adding the total number of endothelial and
837 mesenchymal cells, we obtained a dataset of 25816 cells. Differential expression and
838 differential abundance analyses were carried out on this dataset in the same way as for our
839 bleomycin dataset as described above.
840
841 **Statistical Analysis.**
842 Statistical analyses were performed using GraphPad Prism and R studio (v.4.1.2). Boxplots
843 are given as median ±quartile. Histogram and scatter plot are given as mean ±SD. Two-tailed
844 Mann–Whitney test or multiple paired t test were used for single comparisons; Two-way
845 ANOVA test followed by a multiple comparisons test with Holm-Šídák correction was used for
846 multiple comparisons. P-value <0.05 was considered statistically significant.
847
848 **DATA AVAILABILITY**
849 The scRNA-seq and spatial transcriptomic data sets have been deposited in the Gene
850 Expression Omnibus SuperSerie GSE234199.
851
852 **CODE AVAILABILITY**
853 The scripts used for the analysis of scRNA-seq and spatial transcriptomic data are available
854 on github : https://github.com/marintruchi/Aging_affects_reprogramming_of_PCEC.
855
856

857 **REFERENCES**

858

859 1. Zepp, J.A. & Morrisey, E.E. Cellular crosstalk in the development and regeneration of
860 the respiratory system. *Nat Rev Mol Cell Biol* **20**, 551-566 (2019).
861 2. Wijsenbeek, M. & Cottin, V. Spectrum of Fibrotic Lung Diseases. *N Engl J Med* **383**,
862 958-968 (2020).
863 3. Spagnolo, P. *et al.* Idiopathic pulmonary fibrosis: Disease mechanisms and drug
864 development. *Pharmacol Ther* **222**, 107798 (2021).
865 4. Wolters, P.J., Collard, H.R. & Jones, K.D. Pathogenesis of idiopathic pulmonary
866 fibrosis. *Annu Rev Pathol* **9**, 157-179 (2014).
867 5. Mora, A.L., Bueno, M. & Rojas, M. Mitochondria in the spotlight of aging and idiopathic
868 pulmonary fibrosis. *J Clin Invest* **127**, 405-414 (2017).
869 6. Cho, S.J. & Stout-Delgado, H.W. Aging and Lung Disease. *Annu Rev Physiol* **82**, 433-
870 459 (2020).
871 7. Venosa, A. Senescence in Pulmonary Fibrosis: Between Aging and Exposure. *Front*
872 *Med (Lausanne)* **7**, 606462 (2020).
873 8. Alvarez, D.F. *et al.* Lung microvascular endothelium is enriched with progenitor cells
874 that exhibit vasculogenic capacity. *Am J Physiol Lung Cell Mol Physiol* **294**, L419-430
875 (2008).
876 9. Gillich, A. *et al.* Capillary cell-type specialization in the alveolus. *Nature* **586**, 785-789
877 (2020).
878 10. Ding, B.S. *et al.* Endothelial-derived angiocrine signals induce and sustain regenerative
879 lung alveolarization. *Cell* **147**, 539-553 (2011).
880 11. Vila Ellis, L. *et al.* Epithelial Vegfa Specifies a Distinct Endothelial Population in the
881 Mouse Lung. *Dev Cell* **52**, 617-630 e616 (2020).
882 12. Niethamer, T.K. *et al.* Defining the role of pulmonary endothelial cell heterogeneity in
883 the response to acute lung injury. *Elife* **9** (2020).
884 13. Adams, T.S. *et al.* Single-cell RNA-seq reveals ectopic and aberrant lung-resident cell
885 populations in idiopathic pulmonary fibrosis. *Sci Adv* **6**, eaba1983 (2020).
886 14. Schupp, J.C. *et al.* Integrated Single-Cell Atlas of Endothelial Cells of the Human Lung.
887 *Circulation* **144**, 286-302 (2021).
888 15. de Rooij, L. *et al.* The pulmonary vasculature in lethal COVID-19 and idiopathic
889 pulmonary fibrosis at single-cell resolution. *Cardiovasc Res* **119**, 520-535 (2023).
890 16. Ungvari, Z., Tarantini, S., Donato, A.J., Galvan, V. & Csiszar, A. Mechanisms of
891 Vascular Aging. *Circ Res* **123**, 849-867 (2018).

892 17. Xu, X. *et al.* Age-related Impairment of Vascular Structure and Functions. *Aging Dis* **8**,
893 590-610 (2017).
894 18. Caporarello, N. *et al.* Dysfunctional ERG signaling drives pulmonary vascular aging
895 and persistent fibrosis. *Nat Commun* **13**, 4170 (2022).
896 19. Jenkins, R.G. *et al.* An Official American Thoracic Society Workshop Report: Use of
897 Animal Models for the Preclinical Assessment of Potential Therapies for Pulmonary
898 Fibrosis. *Am J Respir Cell Mol Biol* **56**, 667-679 (2017).
899 20. Redente, E.F. *et al.* Age and sex dimorphisms contribute to the severity of bleomycin-
900 induced lung injury and fibrosis. *Am J Physiol Lung Cell Mol Physiol* **301**, L510-518
901 (2011).
902 21. Stout-Delgado, H.W. *et al.* Age-Dependent Susceptibility to Pulmonary Fibrosis Is
903 Associated with NLRP3 Inflammasome Activation. *Am J Respir Cell Mol Biol* **55**, 252-
904 263 (2016).
905 22. Sueblinvong, V. *et al.* Aging promotes pro-fibrotic matrix production and increases
906 fibrocyte recruitment during acute lung injury. *Adv Biosci Biotechnol* **5**, 19-30 (2014).
907 23. Hecker, L. *et al.* Reversal of persistent fibrosis in aging by targeting Nox4-Nrf2 redox
908 imbalance. *Sci Transl Med* **6**, 231ra247 (2014).
909 24. Caporarello, N. *et al.* Vascular dysfunction in aged mice contributes to persistent lung
910 fibrosis. *Aging Cell* **19**, e13196 (2020).
911 25. Rehan, M. *et al.* Restoration of SIRT3 gene expression by airway delivery resolves
912 age-associated persistent lung fibrosis in mice. *Nat Aging* **1**, 205-217 (2021).
913 26. Liang, J. *et al.* Reciprocal interactions between alveolar progenitor dysfunction and
914 aging promote lung fibrosis. *Elife* **12** (2023).
915 27. Miller, B.F., Huang, F., Atta, L., Sahoo, A. & Fan, J. Reference-free cell type
916 deconvolution of multi-cellular pixel-resolution spatially resolved transcriptomics data.
917 *Nat Commun* **13**, 2339 (2022).
918 28. Goodwin, A.T., Noble, P.W. & Tatler, A.L. Plasma cells: a feasible therapeutic target in
919 pulmonary fibrosis? *Eur Respir J* **60** (2022).
920 29. Kamiya, M. *et al.* Immune mechanisms in fibrotic interstitial lung disease. *Cell* **187**,
921 3506-3530 (2024).
922 30. Stoeckius, M. *et al.* Cell Hashing with barcoded antibodies enables multiplexing and
923 doublet detection for single cell genomics. *Genome Biol* **19**, 224 (2018).
924 31. Joshi, N. *et al.* A spatially restricted fibrotic niche in pulmonary fibrosis is sustained by
925 M-CSF/M-CSFR signalling in monocyte-derived alveolar macrophages. *Eur Respir J*
926 **55** (2020).
927 32. Aran, D. *et al.* Reference-based analysis of lung single-cell sequencing reveals a
928 transitional profibrotic macrophage. *Nat Immunol* **20**, 163-172 (2019).

929 33. Misharin, A.V. *et al.* Monocyte-derived alveolar macrophages drive lung fibrosis and
930 persist in the lung over the life span. *J Exp Med* **214**, 2387-2404 (2017).
931 34. Habermann, A.C. *et al.* Single-cell RNA sequencing reveals profibrotic roles of distinct
932 epithelial and mesenchymal lineages in pulmonary fibrosis. *Sci Adv* **6**, eaba1972
933 (2020).
934 35. Strunz, M. *et al.* Alveolar regeneration through a Krt8+ transitional stem cell state that
935 persists in human lung fibrosis. *Nat Commun* **11**, 3559 (2020).
936 36. Wang, X. *et al.* LRG1 promotes angiogenesis by modulating endothelial TGF-beta
937 signalling. *Nature* **499**, 306-311 (2013).
938 37. Browaeys, R., Saelens, W. & Saeys, Y. NicheNet: modeling intercellular
939 communication by linking ligands to target genes. *Nat Methods* **17**, 159-162 (2020).
940 38. Rafii, S., Butler, J.M. & Ding, B.S. Angiocrine functions of organ-specific endothelial
941 cells. *Nature* **529**, 316-325 (2016).
942 39. Ricard, N., Bailly, S., Guignabert, C. & Simons, M. The quiescent endothelium:
943 signalling pathways regulating organ-specific endothelial normalcy. *Nat Rev Cardiol*
944 **18**, 565-580 (2021).
945 40. Bian, F. *et al.* Lung endothelial cells regulate pulmonary fibrosis through FOXF1/R-Ras
946 signaling. *Nat Commun* **14**, 2560 (2023).
947 41. Sauler, M., Bucala, R. & Lee, P.J. Role of macrophage migration inhibitory factor in
948 age-related lung disease. *Am J Physiol Lung Cell Mol Physiol* **309**, L1-10 (2015).
949 42. Xu, S. *et al.* The zinc finger transcription factor, KLF2, protects against COVID-19
950 associated endothelial dysfunction. *Signal Transduct Target Ther* **6**, 266 (2021).
951 43. Huang, L.T. *et al.* Klf10 deficiency in mice exacerbates pulmonary inflammation by
952 increasing expression of the proinflammatory molecule NPRA. *Int J Biochem Cell Biol*
953 **79**, 231-238 (2016).
954 44. Malinverno, M. *et al.* Peg3/PW1 Is a Marker of a Subset of Vessel Associated
955 Endothelial Progenitors. *Stem Cells* **35**, 1328-1340 (2017).
956 45. Bergen, V., Lange, M., Peidli, S., Wolf, F.A. & Theis, F.J. Generalizing RNA velocity to
957 transient cell states through dynamical modeling. *Nat Biotechnol* **38**, 1408-1414 (2020).
958 46. Tsukui, T. *et al.* Collagen-producing lung cell atlas identifies multiple subsets with
959 distinct localization and relevance to fibrosis. *Nat Commun* **11**, 1920 (2020).
960 47. Camilli, C., Hoeh, A.E., De Rossi, G., Moss, S.E. & Greenwood, J. LRG1: an emerging
961 player in disease pathogenesis. *J Biomed Sci* **29**, 6 (2022).
962 48. Liu, C. *et al.* Collaborative Regulation of LRG1 by TGF-beta1 and PPAR-beta/delta
963 Modulates Chronic Pressure Overload-Induced Cardiac Fibrosis. *Circ Heart Fail* **12**,
964 e005962 (2019).

49. Sng, M.K. *et al.* Selective deletion of PPARbeta/delta in fibroblasts causes dermal fibrosis by attenuated LRG1 expression. *Cell Discov* **4**, 15 (2018).
50. Honda, H. *et al.* Leucine-rich alpha-2 glycoprotein promotes lung fibrosis by modulating TGF-beta signaling in fibroblasts. *Physiol Rep* **5** (2017).
51. Zhao, G. *et al.* TGF-betaR2 signaling coordinates pulmonary vascular repair after viral injury in mice and human tissue. *Sci Transl Med* **16**, eadg6229 (2024).
52. Liu, M. *et al.* Sox17 is required for endothelial regeneration following inflammation-induced vascular injury. *Nat Commun* **10**, 2126 (2019).
53. Marsboom, G. & Rehman, J. Hypoxia Signaling in Vascular Homeostasis. *Physiology (Bethesda)* **33**, 328-337 (2018).
54. Lang, N.J. *et al.* Ex vivo tissue perturbations coupled to single-cell RNA-seq reveal multilineage cell circuit dynamics in human lung fibrogenesis. *Sci Transl Med* **15**, eadh0908 (2023).
55. Raslan, A.A. *et al.* Lung injury-induced activated endothelial cell states persist in aging-associated progressive fibrosis. *Nat Commun* **15**, 5449 (2024).
56. Savary, G. *et al.* The Long Non-Coding RNA DNM3OS is a Reservoir of FibromiRs with Major Functions in Lung Fibroblast Response to TGF-beta and Pulmonary Fibrosis. *Am J Respir Crit Care Med* (2019).
57. Righelli, D. *et al.* SpatialExperiment: infrastructure for spatially-resolved transcriptomics data in R using Bioconductor. *Bioinformatics* **38**, 3128-3131 (2022).
58. Angelidis, I. *et al.* An atlas of the aging lung mapped by single cell transcriptomics and deep tissue proteomics. *Nat Commun* **10**, 963 (2019).

Acknowledgements: The authors thank the technical support of the UCA GenomiX, the CoBioDA bioinformatics hub of the IPMC and the microscopy facility from the IPMC, part of the « Microscopie Imagerie Cytométrie Azur» GIS IBiSA labeled platform. We also thank the staffs from the Nice Hospital-Integrated Biobank (BB-0033-00025) and the Giessen PNEUMObank as well as from the animal care facilities institutions at Sophia Antipolis (IPMC Animal Care Facility) and Lille (High Technology Animal Care Facility, University of Lille 2). We are also grateful to A. Monteil and C. Lemmers from the Vectorology facility, PVM, Biocampus Montpellier, CNRS UMS3426. We acknowledge the support from the Centre National de la Recherche Scientifique (CNRS), Institut National de la Santé et de la Recherche Médicale (Inserm), Université Côte d'Azur, Université de Lille, the French Government, through the National Research Agency (ANR) programs ANR-PRCI-18-CE92-0009-01 FIBROMIR / ANR-22-CE17-0046-01 MIR-ASO and the UCAJ.E.D.I. Investments in the Future project with the reference number ANR-15-IDEX-01, the Programme Contrat Plan État Région (CPER) - CTRL

(Centre Transdisciplinaire de Recherche sur la Longévité, projet FISSURE) as well as Canceropôle PACA.

Author contributions.

BM, NP, GV and CC conceived and designed the study and supervised the entire work. MT and BM wrote the manuscript. GS, MGI, HC and AB performed in vivo studies. GS, MGI, HC, JF, NB and CdS performed biochemical and cellular biology experiments. GS, CdS and MJA performed the Visium spatial transcriptomic experiment. VM and CGR generated scRNA-seq data and primary analysis. MT performed bioinformatic analysis of scRNA-seq and spatial transcriptomic data. KLB co-supervised the computational analysis. GS, MGI, RL and HC performed and analyzed immunostainings. MT, GS, AL, NR, GV, CC, SB, NP and BM performed biological interpretation. VH, PH, AG, CHM and SL provided IPF-derived biological materials and contributed to biological interpretation of data. RR, MP, NR, PB and SB gave conceptual advices. OP and SB provided ressources. All authors read and corrected the final manuscript.

Competing interests.

None declared

1020 **Table 1. Main markers of Lrg1^{pos} PCEC subpopulations.**

Subpopulation	marker	description
sCap	Ccnd1	cyclin D1
	Cd34	CD34 antigen
	Col15a1	collagen, type XV, alpha 1
	F2r	coagulation factor II (thrombin) receptor
	Fscn1	fascin actin-bundling protein 1
	Hspg2	perlecan (heparan sulfate proteoglycan 2)
	Igfbp7	insulin-like growth factor binding protein 7
	Ivns1abp	influenza virus NS1A binding protein
	Nrp2	neuropilin 2
	Plxnd1	plexin D1
	Rflnb	refilin B
	Rgcc	regulator of cell cycle
	Trp53i11	transformation related protein 53 inducible protein 11
sCap, Lrg1^{pos} gCap	Sparcl1	SPARC-like 1
Lrg1^{pos} gCap	Ackr3	atypical chemokine receptor 3
	Atp8b1	ATPase, class I, type 8B, member 1
	Cmah	cytidine monophospho-N-acetylneuraminic acid hydroxylase
	Gadd45g	growth arrest and DNA-damage-inducible 45 gamma
	Mctp1	multiple C2 domains, transmembrane 1
	Ntrk2	neurotrophic tyrosine kinase, receptor, type 2
	Plac8	placenta-specific 8
	Scarb1	scavenger receptor class B, member 1
	Scn3b	sodium channel, voltage-gated, type III, beta
	Sparcl1	SPARC-like 1
	Tiam1	T cell lymphoma invasion and metastasis 1
	Tmem252	transmembrane protein 252
Lrg1^{pos} gCap, Lrg1^{pos} aCap	Ankrd37	ankyrin repeat domain 37
	Lrg1	leucine-rich alpha-2-glycoprotein 1
Lrg1^{pos} aCap	Adora2a	adenosine A2a receptor
	Apln	apelin
	Bdkrb2	bradykinin receptor, beta 2
	Bnip3	BCL2/adenovirus E1B interacting protein 3
	Ccdc184	coiled-coil domain containing 184
	Chst1	carbohydrate sulfotransferase 1
	Dnah11	dynein, axonemal, heavy chain 11
	F2r	coagulation factor II (thrombin) receptor
	Fgfr1	fibroblast growth factor receptor 1
	Meox1	mesenchyme homeobox 1
	Ncam1	neural cell adhesion molecule 1
	Serpine1	serine (or cysteine) peptidase inhibitor, clade E, member 1
	Tnfrsf11b	tumor necrosis factor receptor superfamily, member 11b

1021

1022 **Table 2. Commonly regulated genes in systemic EC from IPF samples and from**
1023 **bleomycin model.**

gene symbol (hsa)	description	function	expression_in_fibrosis
ACVRL1	activin A receptor like type 1	Angiogenesis	downregulated
APLN	apelin	Angiogenesis	upregulated
APLNR	apelin receptor	Angiogenesis	upregulated
BMPR2	bone morphogenetic protein receptor type 2	Angiogenesis	downregulated
FLT4	fms related receptor tyrosine kinase 4	Angiogenesis	upregulated
KDR	kinase insert domain receptor	Angiogenesis	upregulated
TEK	TEK receptor tyrosine kinase	Angiogenesis	downregulated
THBS1	thrombospondin 1	Angiogenesis	upregulated
TMEM100	transmembrane protein 100	Angiogenesis	downregulated
VEGFC	vascular endothelial growth factor C	Angiogenesis	downregulated
SRGN	serglycin	Apoptosis	downregulated
TNFRSF10B	TNF receptor superfamily member 10b	Apoptosis	upregulated
THBD	thrombomodulin	Blood coagulation	downregulated
CD34	CD34 molecule	Cell adhesion	upregulated
IGFBP7	insulin like growth factor binding protein 7	Cell adhesion	upregulated
LAMA4	laminin subunit alpha 4	Cell adhesion	upregulated
LAMB1	laminin subunit beta 1	Cell adhesion	upregulated
LAMC1	laminin subunit gamma 1	Cell adhesion	upregulated
STXBP6	syntaxin binding protein 6	Cell adhesion	downregulated
VWF	von Willebrand factor	Cell adhesion, Blood coagulation	downregulated
SORBS1	sorbin and SH3 domain containing 1	Cell adhesion, Cell signaling	downregulated
CCND1	cyclin D1	Cell cycle	upregulated
RASSF2	Ras association domain family member 2	Cell cycle	upregulated
RGCC	regulator of cell cycle	Cell cycle	upregulated
DUSP1	dual specificity phosphatase 1	Cell cycle, Stress response	downregulated
FGFR3	fibroblast growth factor receptor 3	Cell proliferation	downregulated
INHBB	inhibin subunit beta B	Cell signaling	upregulated
GJA1	gap junction protein alpha 1	Cell-cell communication	upregulated
ENPP2	ectonucleotide pyrophosphatase/phosphodiesterase 2	Chemotaxis, Lipid metabolism	upregulated
CXCL12	C-X-C motif chemokine ligand 12	Cytokine	upregulated
INMT	indolethylamine N-methyltransferase	Detoxification	downregulated
ABI3BP	ABI family member 3 binding protein	ECM organisation	downregulated
ADGRG6	adhesion G protein-coupled receptor G6	ECM organisation	downregulated
COL15A1	collagen type XV alpha 1 chain	ECM organisation	upregulated
COL4A1	collagen type IV alpha 1 chain	ECM organisation	upregulated
COL4A2	collagen type IV alpha 2 chain	ECM organisation	upregulated
ELN	elastin	ECM organisation	downregulated
SPARC	secreted protein acidic and cysteine rich	ECM organisation	upregulated
VWA1	von Willebrand factor A domain containing 1	ECM organisation	upregulated

PDGFB	platelet derived growth factor subunit B	Growth factor	upregulated
TGFB2	transforming growth factor beta 2	Growth factor	downregulated
ARL4D	ADP ribosylation factor like GTPase 4D	Intracellular trafficking	downregulated
MGLL	monoglyceride lipase	Lipid metabolism	upregulated
PTGIS	prostaglandin I2 synthase	Lipid metabolism	downregulated
PTGS1	prostaglandin-endoperoxide synthase 1	Lipid metabolism	downregulated
TIMP3	TIMP metallopeptidase inhibitor 3	Metalloprotease inhibitor	downregulated
ANXA3	annexin A3	Phospholipase A2 inhibitor	downregulated
SPRY1	sprouty RTK signaling antagonist 1	Regulation of growth factor	upregulated
ANKRD44	ankyrin repeat domain 44	regulation of PP6 complex	downregulated
LTBP1	latent TGFB binding protein 1	Regulation of TGF-B	downregulated
NREP	neuronal regeneration related protein	Regulation of TGF-B	upregulated
CRYAB	crystallin alpha B	Stress response	downregulated
PDLIM1	PDZ and LIM domain 1	Stress response	upregulated
CEBPD	CCAAT enhancer binding protein delta	Transcription regulation	downregulated
EBF1	EBF transcription factor 1	Transcription regulation	upregulated
FOXF1	forkhead box F1	Transcription regulation	downregulated
GATA2	GATA binding protein 2	Transcription regulation	downregulated
GATA6	GATA binding protein 6	Transcription regulation	downregulated
HDAC9	histone deacetylase 9	Transcription regulation	downregulated
HES1	hes family bHLH transcription factor 1	Transcription regulation	downregulated
HIF1A	hypoxia inducible factor 1 subunit alpha	Transcription regulation	upregulated
KLF2	KLF transcription factor 2	Transcription regulation	downregulated
KLF4	KLF transcription factor 4	Transcription regulation	downregulated
KLF9	KLF transcription factor 9	Transcription regulation	downregulated
MEOX1	mesenchyme homeobox 1	Transcription regulation	upregulated
PRDM1	PR/SET domain 1	Transcription regulation	upregulated
SMAD1	SMAD family member 1	Transcription regulation	upregulated
SMAD6	SMAD family member 6	Transcription regulation	downregulated
SMAD7	SMAD family member 7	Transcription regulation	downregulated
SOX17	SRY-box transcription factor 17	Transcription regulation	upregulated
SOX4	SRY-box transcription factor 4	Transcription regulation	upregulated
EMP3	epithelial membrane protein 3	Transmembrane signaling	downregulated
FAM13C	family with sequence similarity 13 member C	Unknown	upregulated
SAMD5	sterile alpha motif domain containing 5	Unknown	downregulated
TM6SF1	transmembrane 6 superfamily member 1	Unknown	downregulated

1024

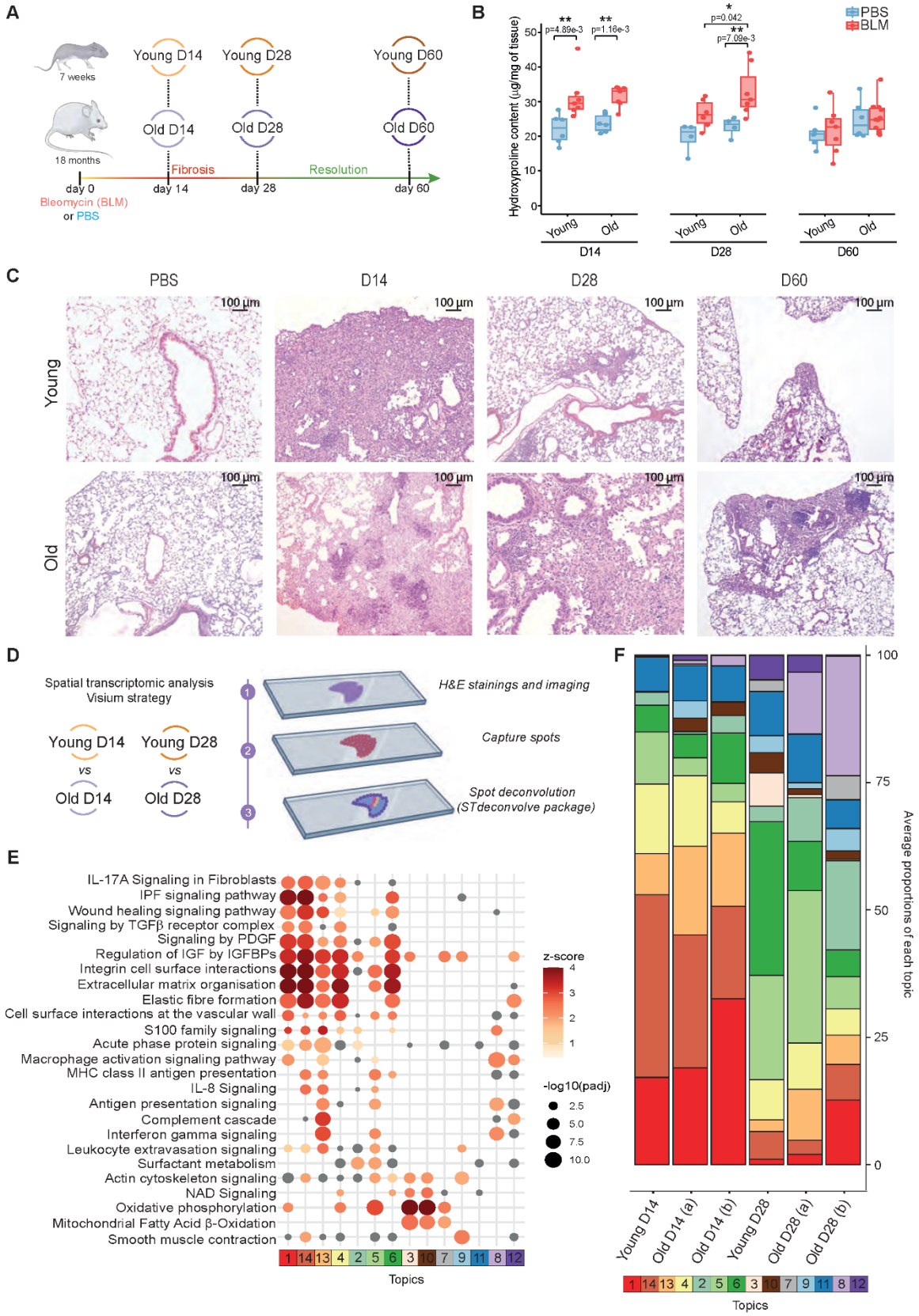

Figure 1. Analyses of fibrotic parameters in bleomycin-injured lungs from young and old mice. (A) Experimental design. Young (7 weeks) or old (18 months) mice were treated either with bleomycin (BLM) or PBS. Their lungs were collected at the bleomycin-induced fibrotic peak at day 14 and during lung regeneration (day 28) and fibrosis resolution (day 60). **(B)** Hydroxyproline quantification on BLM or PBS treated young or old mouse samples at indicated time points (n=4-10/group). * P<0.05. ** P<0.01. P values were calculated by two-way ANOVA test followed by a multiple comparisons test with Holm-Šídák correction. **(C)** Histological sections of control and fibrotic lungs from young and old mice using H&E at indicated time points (representative images, n=3). **(D)** Experimental design of spatial transcriptomics data from histological sections (H&E) of lungs from young (n=1) and old (n=2) mice challenged with bleomycin and collected at fibrotic peak (day 14, D14) and during regeneration (day 28, D28). Spots captured corresponding to tissue area were deconvoluted through ST deconvolve package in topics (n=14). **(E)** Functional annotations of topics by Ingenuity pathway. **(F)** Average proportion of each topic across deconvoluted spots in each slice.

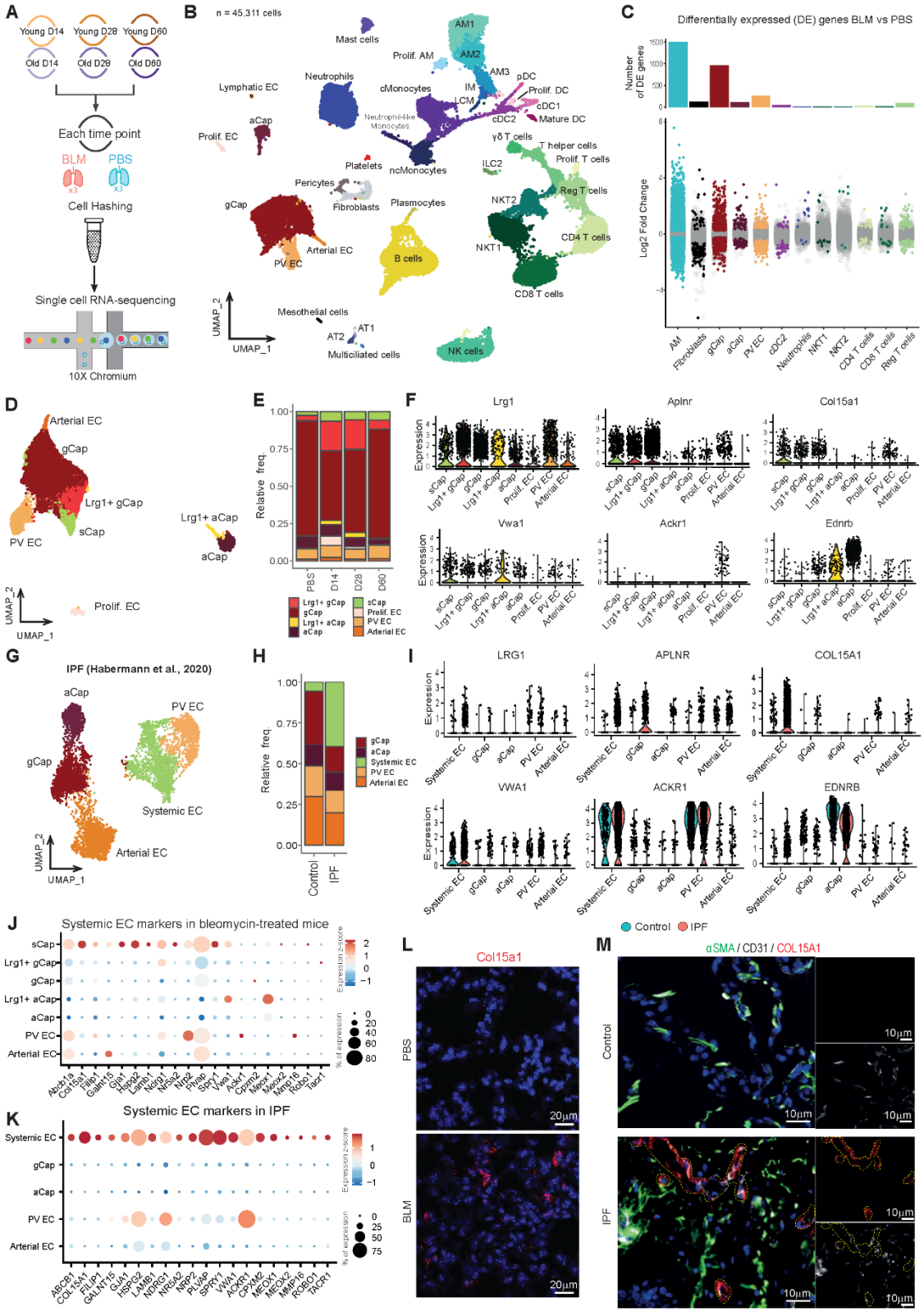

Figure 2. Time-resolved scRNA-seq captures pulmonary cell populations heterogeneity in bleomycin-injured lungs from young and old mice. (A) scRNA-seq experimental design (n=3, for each experimental condition at each time point). **(B)** UMAP of the integrated dataset of the 45311 sequenced cells. Cells are colored according to the annotated clusters. Prolif. AM = proliferating macrophages; AM = alveolar macrophages; IM = interstitial macrophages; LCM = large-cavity macrophages; Prolif. DC = proliferating dendritic cells; cDC = conventional dendritic cell; Mature DC = mature dendritic cells; pDC = plasmacytoid dendritic cells; cMonocytes/ncMonocytes = conventional/non-conventional monocytes; Prolif. T cells = proliferating T cells; Reg T cells = regulatory T cells; ILC2 = type 2 innate lymphoid cells; NKT = natural killer T cells; NK cells = natural killer; AT1/2 = Alveolar Type 1/2 cells. **(C)** Differentially expressed genes (DEGs) between Bleomycin and PBS treated cells for indicated populations. The number of DEGs is limited to 1500 for the bar plot. **(D)** UMAP of pulmonary EC subpopulations. gCap = general capillaries cells, aCap = aerocytes capillary endothelial cells, sCap = systemic capillary endothelial cells, PV EC = pulmonary-venous endothelial cells. **(E)** Relative proportions of PCEC subpopulations across time points. **(F)** Normalized expression of *Col15a1, Lrg1, Aplnr, Vwa1, Ackr1* and *Ednrb*. **(G)** UMAP of EC subpopulations from Habermann et al. dataset. **(H)** Relative proportion of EC subpopulations from Habermann et al. dataset. **(I)** Normalized expression of *LRG1, COL15A1, VWA1, ACKR1, APLNR* and *EDNRB* in EC subpopulations from control (blue) and IPF (light red) samples from Habermann et al. dataset. **(J-K)** Systemic EC markers comparison between mice **(J)** and human **(K)** fibrosis. **(L)** *In situ* hybridization of *Col15a1* mRNA in BLM or PBS conditions. **(M)** Expression of COL15A1 in lung sections from normal or IPF tissues by Immunofluorescence. Representative immunofluorescent images of COL15A1 (in red) with the pan EC marker CD31 (white) and αSMA (green). Nuclei are counterstained with DAPI. (n=5).

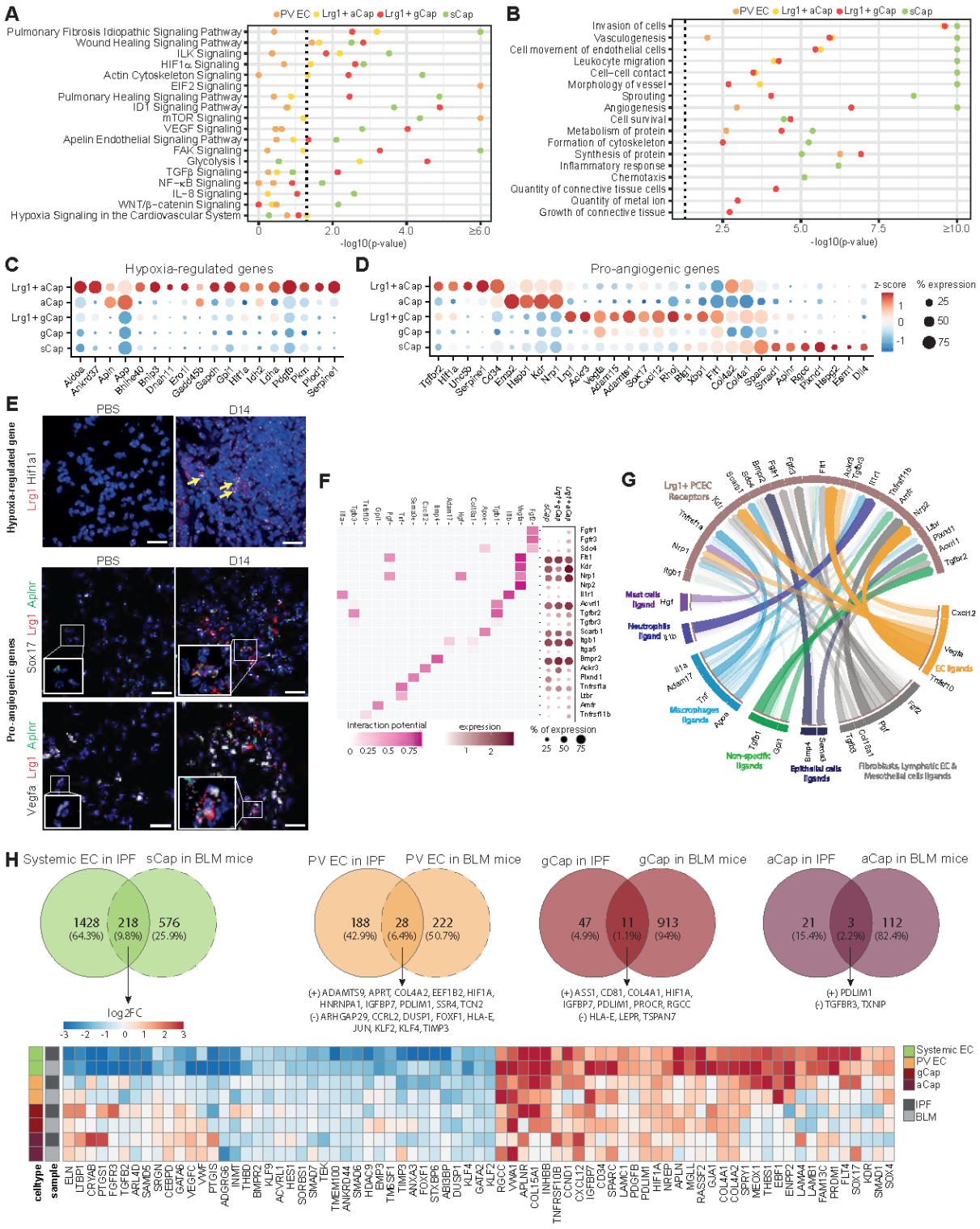

Figure 3. Lung injury shift pulmonary endothelial cells towards *Lrg1*^{pos} subpopulations associated with lung alveolar niche regeneration. (A) Selection of top activated canonical pathways in *Lrg1*^{pos} PCEC subpopulations. **(B)** Selection of top activated functions in *Lrg1*^{pos} PCEC subpopulations. **(C-D)** Level and percentage of expression of hypoxia-regulated (C) and pro-angiogenic (D) genes in *Lrg1*^{pos} PCEC subpopulations. **(E)** RNA FISH acquisition for *Hif1a1* (black, top), *Sox17* (black, middle), *Vegfa* (black, down), *Aplnr* (green) and *Lrg1* (red) mRNA in PBS or D14 in young mice. Scale bars =20µm. **(F)** Interaction potential between the prioritized ligands and their *bona fide* receptors (left); Level and percentage of expression of each receptor in *Lrg1*^{pos} PCEC subpopulations (right) **(G)** Circos plot of ligands-receptors interactions predicted by NicheNet analysis. Ligands are colored according to their specific expression. **(H)** Comparison of human and mouse pulmonary fibrosis signatures in Systemic EC, PV EC, gCap and aCap. Log2FC of similarly modulated genes in murine sCap and human systemic EC are displayed in the heatmap.

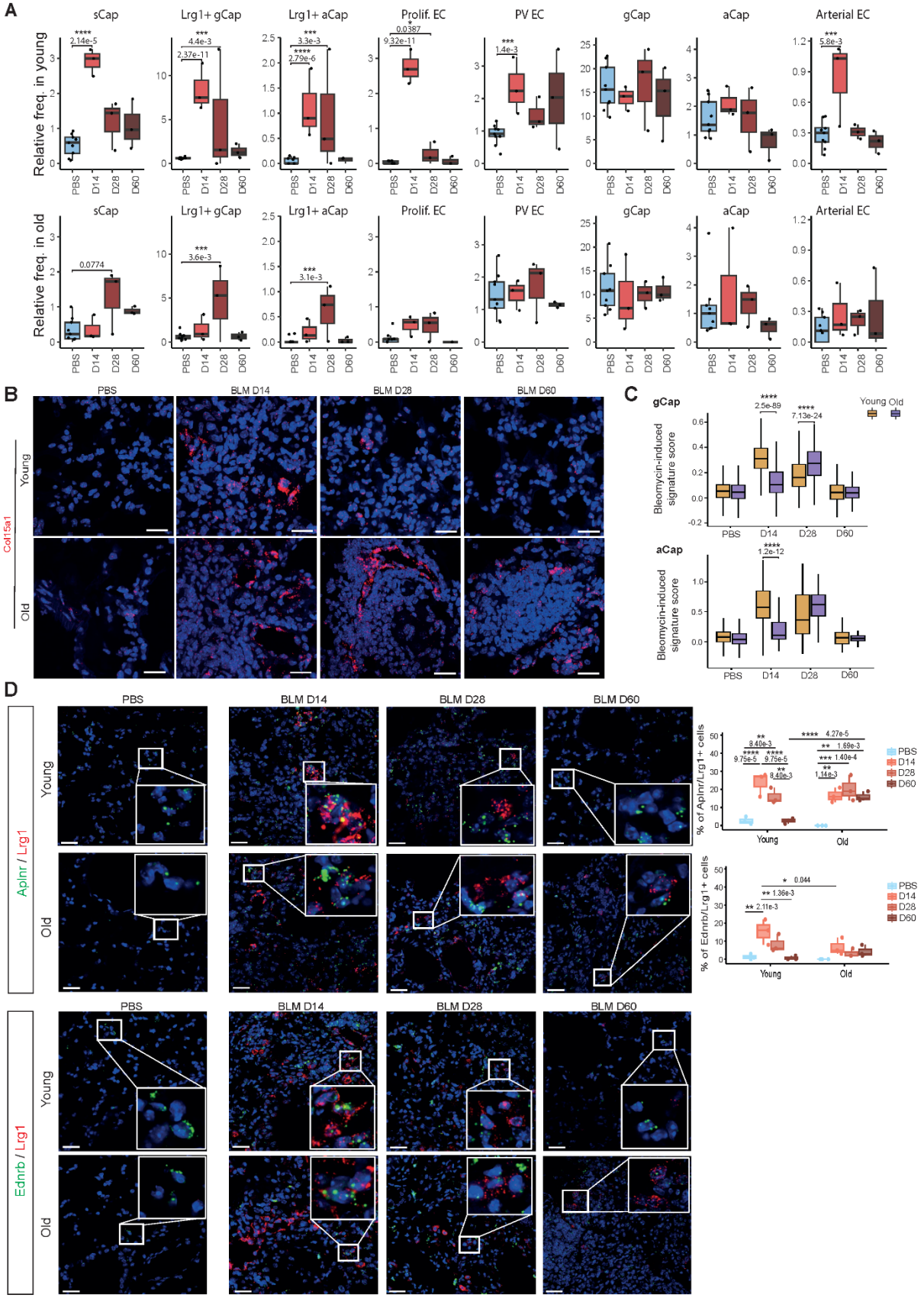

Figure 4. *Lrg1*^{pos} PCEC dynamics are delayed in old mice. (A) Pulmonary endothelial subpopulations relative frequencies in young and old mice across time points. **(B)** *In situ* hybridization of *Col15a1* mRNA at indicated time points in young and old mice. Scale bars = 20µm. **(C)** Bleomycin (BLM)-induced signature score (see material and methods section) in gCap (top) and aCap (bottom) in young and old mice across time points. **(D)** *In situ* hybridization of *Lrg1* mRNA with gCap marker *Aplnr* mRNA or aCap marker *Ednrb* mRNA at indicated time points in young and old mice. (n=3 independent mice, 3 counted microscopic fields / mouse, scale bars =20µm). Quantification was performed in three different fields for each mouse. * P<0.05, ** P<0.01, *** P<0.001, **** P<0.0001. P values were calculated by a Two-way ANOVA test followed by a multiple comparisons test with Holm-Sidak correction.

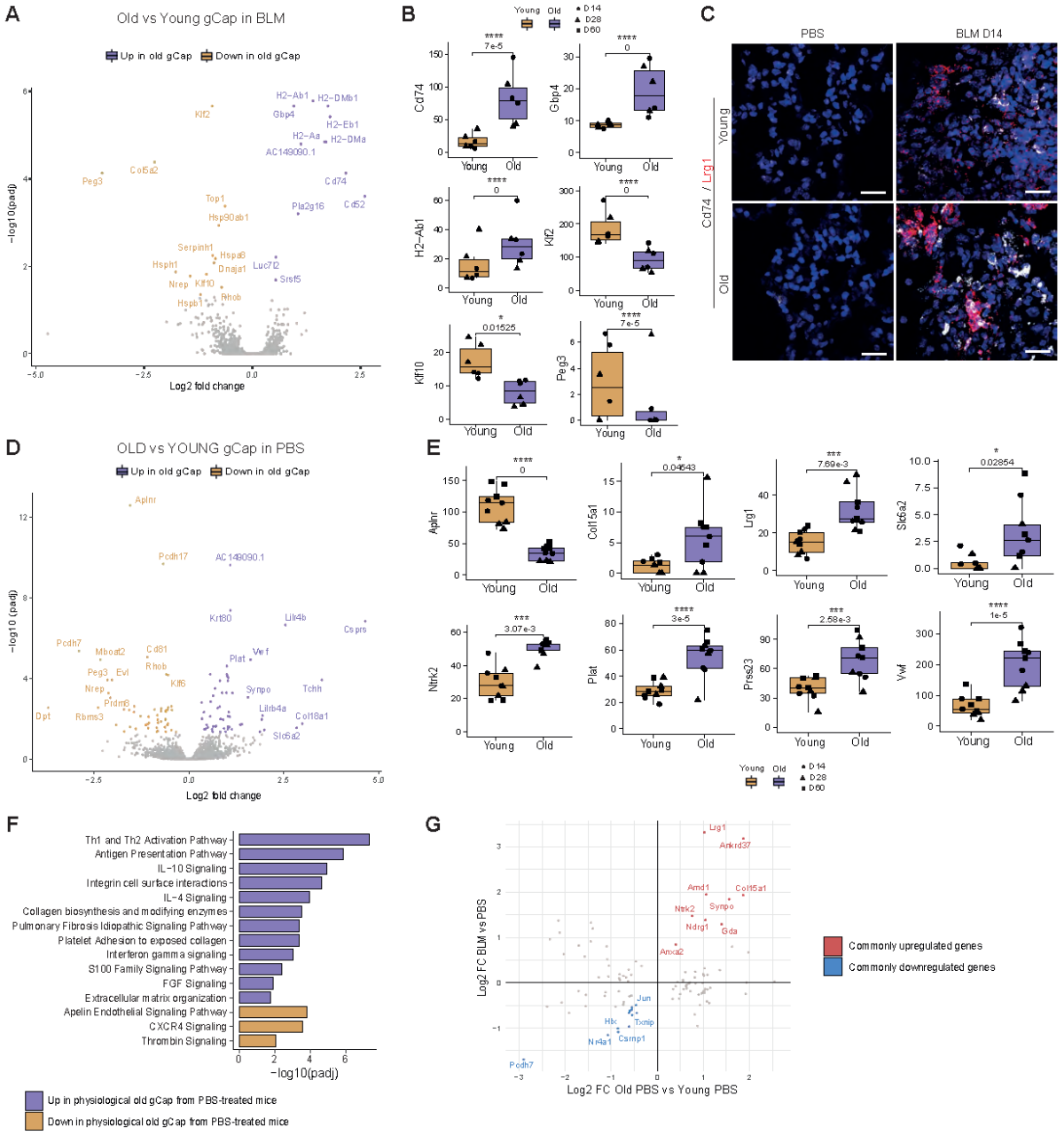

Figure 5. Aged mouse lung gCap exhibit pro-inflammatory and injury-activated phenotype. (A) Differentially expressed genes (DEGs) between old and young gCap in fibrotic condition. **(B)** Expression of several genes dysregulated in age-related in gCap under BLM conditions (*Cd74, Gbp4, H2-Ab1, Klf2, Klf10* and *Peg3*). Boxplot of relative expression, each point corresponds to a mice (● for D14, ▲ for D28 and ■ for D60). **(C)** *In situ* hybridization of *Cd74* mRNA in BLM or Day 14 after bleomycin induction in young and old mice. Scale bars = 20µm. **(D)** DEGs between old and young gCap in physiological condition. **(E)** Expression of several genes dysregulated in age-related in gCap under PBS conditions (*Aplnr, Col15a1, Lrg1, Slc6a2, Ntrk2, Plat, Prss23* and *Vwf*). Boxplot of relative expression, each point corresponds to a mice (● for D14, ▲ for D28 and ■ for D60). **(F)** Function enrichment analysis on DEGs between old and young physiological gCap. (**G**) Expression of several age-related dysregulated genes in gCap under BLM/PBS conditions.

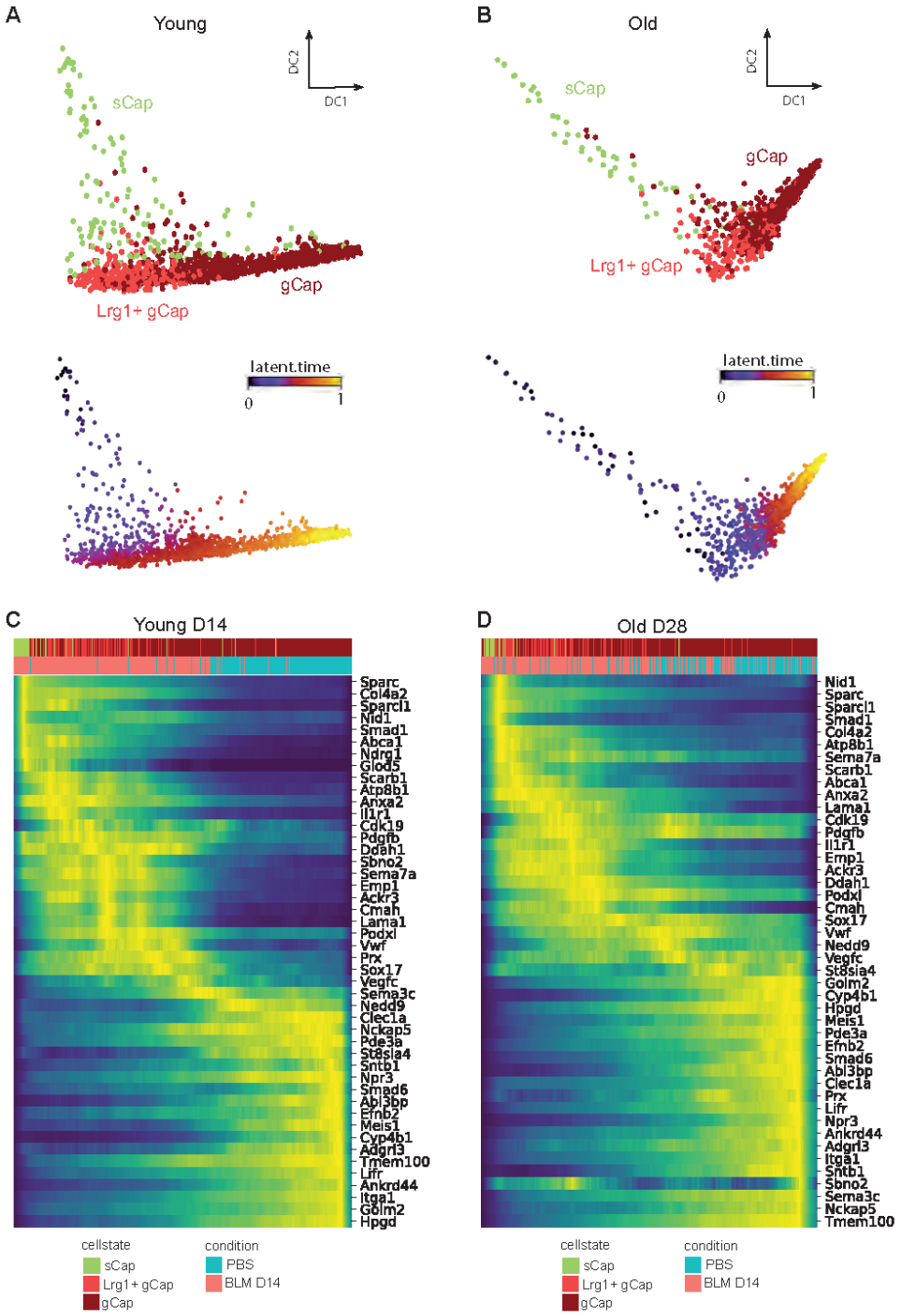

Figure 6. RNA velocity analysis reveals transcriptional dynamics of PCEC during alveolar regeneration. (A-B) Diffusion map computed on Young D14 **(A)** or old D28 **(B)** mouse spliced RNA data (3 Bleomycin and 3 PBS-treated mice), with cells colored according to PCEC subpopulation (up) and RNA velocity latent time (bottom). **(C-D)** Heatmap of the top contributing genes to the transcriptional dynamic, with cells ordered by latent time in young D14 **(C)** or old D28 **(D)** mice.

1093 **Supplementary information**

1094

1095 **Correspondence of supplementary tables:**

1096 **Supplementary table S1.** Differential expression analysis between topics deconvoluted from
1097 spatial transcriptomic data.

1098 **Supplementary table S2.** Differential expression analysis (Seurat) between annotated
1099 subpopulations of single cell RNA-seq data.

1100 **Supplementary table S3.** Differential expression analysis (DESeq2) between lung cell types
1101 from bleomycin-treated and PBS-treated mice.

1102 **Supplementary table S4.** Differential expression analysis (DESeq2) between IPF patients
1103 and healthy control for aCap, gCap, systemic EC and PV EC, from the Habermann et al.
1104 Dataset[34].

1105 **Supplementary table S5.** Differential expression analysis (DESeq2) between old and young
1106 aCap, gCap and PVEC cells in fibrotic condition.

1107 **Supplementary table S6.** Differential expression analysis (DESeq2) between old and young
1108 aCap, gCap and PVEC cells in physiological condition.

1109

1110 **Correspondence of supplemental Figures:**

1111 **Supplemental Figure S1. Histological and spatial transcriptomics data integration of**
1112 **injured lung slices from young and old mice.**

1113 **Supplemental Figure S2. scRNA-seq analysis of young and aged mouse lungs following**
1114 **BLM challenge at 3 time points.**

1115 **Supplemental Figure S3. Lrg1 expression in lung cell populations.**

1116 **Supplemental Figure S4. LRG1 affects the TGF-β signalling towards a pro-angiogenic**
1117 **response.**

1118 **Supplemental Figure S5. Bleomycin-induced PCEC subpopulations are associated**
1119 **with pro-angiogenic signaling.**

1120 **Supplemental Figure S6. Expression of bleomycin-associated signatures in PCEC from**
1121 **young and aged mouse lungs.**

1122 **Supplemental Figure S7. Expression of selected genes according to RNA Velocity latent**
1123 **time analysis of PVEC subpopulations**.

1124

1125

1126

1127

1128

1129